*Geophys. J. Int.* (1994) **118,** 529–554

# A 57 Ma Pacific plate palaeomagnetic pole determined from a skewness analysis of crossings of marine magnetic anomaly 25r

Katerina E. Petronotis,[1,*] Richard G. Gordon[2,†] and Gary D. Acton[1,*]

[1] *Department of Earth and Planetary Sciences, University of New Mexico, Albuquerque, New Mexico* 87131, *USA*
[2] *Laboratoire de Géodynamique Sous-Marine,* BP 48, 06230 *Villefranche sur Mer, France*

Accepted 1994 January 26. Received 1994 January 25; in original form 1993 June 3

## SUMMARY

An increase in the accuracy and age resolution of the apparent polar wander path of the Pacific plate could be important for testing reconstructions that relate the motion of Pacific basin plates to other plates, for testing if hotspots in different ocean basins are stationary relative to one another, and for estimating the motion of hotspots relative to the spin axis. With these goals in mind, herein we investigate how accurately a palaeomagnetic pole can be estimated from skewness analysis of many crossings of a single magnetic anomaly on the Pacific plate. Apparent effective remanent inclinations of the sea-floor magnetization were estimated from the skewnesses of 132 useful (out of 149 total) crossings of anomaly 25r (56.5–57.8 Ma) distributed over a distance of more than 11 000 km across the Pacific plate. These estimates were inverted to obtain a best-fitting palaeomagnetic pole latitude, pole longitude, and anomalous skewness for this single reversed-polarity chron. The best-fitting model gives a pole of 78.2°N, 4.8°E with a 95 per cent confidence ellipse having a 6.4° major semi-axis oriented 93° clockwise of north and a 4.1° minor semi-axis; anomalous skewness is 16.2° ± 4.6° (95 per cent confidence limits). We also investigated the effect of the dependence of anomalous skewness on spreading rate by correcting our data using an empirical model. The pole obtained from the inversion of this alternative data set lies a statistically insignificant 0.6° from the pole obtained using no correction. That a pole with usefully compact confidence limits and a narrowly resolved, precisely estimated age can be so determined suggests that an accurate apparent polar wander path with a fine-age resolution can be determined for the Pacific plate by applying the same approach to the shapes of other marine magnetic anomalies.

Comparison of our chron 25r pole with other Pacific palaeomagnetic and palaeoequatorial sediment facies data indicates that the Pacific plate remained nearly stationary relative to the spin axis during the Eocene ($-0.05° \text{ Myr}^{-1} \pm 0.28° \text{ Myr}^{-1}$), but probably moved rapidly northward during the Paleocene ($0.83° \text{ Myr}^{-1} \pm 0.46° \text{ Myr}^{-1}$). Comparison of these data to latitudes of dated volcanic edifices along the Hawaiian–Emperor chain indicates that the Hawaiian hotspot drifted southward by 10.2° ± 3.4° (95 per cent confidence limits) since 57 Ma, but only by 1.7° ± 1.9° since 39 Ma, which gives a southward displacement of 8.5° ± 3.9° (95 per cent confidence limits) between 57 and 39 Ma, corresponding to a rate of southward motion of $52 \pm 24 \text{ mm yr}^{-1}$. Incorporation of realistic uncertainties of volcano ages would increase these uncertainties considerably, however. We also examined the distance between the crossings of anomalies 25 and 27 on all the profiles we analysed; along the palaeo-Pacific–Farallon boundary these distances are inconsistent with the joint hypotheses of symmetric spreading and single Pacific and Farallon plates between 62 and 56 Ma, indicating that the evidence for a single Pacific plate in early Tertiary time is not as compelling as it had previously seemed.

* Now at: Department of Geology and Geophysics, University of New England, Armidale, New South Wales 2351, Australia.
† Permanent address: Department of Geological Sciences, Northwestern University, Evanston, Illinois 60208, USA.

**Key words:** anomalous skewness, hotspots, marine magnetic anomalies, palaeomagnetic poles.

## INTRODUCTION

Marine magnetic anomalies over Pacific plate sea-floor provide a continuous record of the palaeomagnetic field from the Jurassic to the present. The relative ages in millions of years of these anomalies are known well. Thus, skewness data from these anomalies may have the potential to provide an apparent polar wander (APW) path with a fine age resolution. Efforts to obtain APW paths from skewness data, which are determined by analysing the shape of the anomalies, have been hampered by an apparently systematic discrepancy called anomalous skewness (Weissel & Hayes 1972; Cande 1976; Cande & Kent 1976; Cande & Kristoffersen 1977; Cande 1978). In a prior paper we presented a method for simultaneously estimating a best-fitting palaeomagnetic pole and the amount of anomalous skewness present in skewness data from a single plate (Petronotis, Gordon & Acton 1992). Because anomalous skewness likely varies significantly between different anomalies (Cande & Kristoffersen 1977; Petronotis & Gordon 1989), the bias ideally should be removed by the analysis of skewness data from many crossings of the same anomaly without incorporating data from crossings of any other anomalies. Regardless of the complexities of age-varying anomalous skewness, obtaining an accurate palaeomagnetic pole from a narrow, well-dated age span is highly desirable. Our main goal herein is to investigate whether a palaeomagnetic pole with usefully compact confidence limits can be obtained from the analysis of the skewness of many crossings of a single magnetic anomaly, in this case anomaly 25r, which is the anomaly corresponding to chron 25r (56.5–57.8 Ma on the time-scale of Cande & Kent 1992, which is used throughout this paper). Chron 25r is the reversed-polarity chron older than normal-polarity chron 25 and younger than normal-polarity chron 26.

Here we present skewness analysis of 149 crossings of anomaly 25r over sea-floor formed by Pacific–Kula, Pacific–Farallon, Pacific–Bellingshausen or Pacific–Antarctic spreading. These phase shifts were converted to apparent effective remanent inclinations (Petronotis *et al.* 1992), which were in turn used to compute a palaeomagnetic pole and anomalous skewness for chron 25r. We chose anomaly 25r for our study for several reasons. There is no Pacific plate pole of comparable age; thus its study could fill an important age gap in the Pacific APW path. Anomaly 25r is the youngest anomaly that was both formed by Pacific–Kula spreading and was long enough to be suitable for skewness analysis. Many Cainozoic and Late Cretaceous chrons are as long or longer than chron 25r, which is 1.3 Myr long. Thus, if we could obtain a useful pole from chron 25r, it would establish the likelihood that useful poles could be similarly obtained for many Cainozoic and Late Cretaceous chrons.

As reported herein, it appears that we have indeed estimated a useful pole for chron 25r. The new pole lies near the Pacific plate 39 Ma pole (Sager 1987) and thus suggests that the Pacific plate moved little, if at all, relative to Earth's rotation axis for 18 Myr during the Eocene. A comparison of the northward motion of the Pacific plate suggested by the chron 25r pole and other APW path data to that, inferred from the progression of dated volcanic edifices along the Hawaiian–Emperor chain indicates that much if not all of the Cainozoic southward drift of the Hawaiian hotspot (Kono 1980; Prince, Heath & Kominz 1980; Suárez & Molnar 1980; Gordon & Cape 1981; Sager 1983, 1987) occurred during the interval 57–39 Ma.

## METHODS

### Obtaining apparent effective inclinations from marine magnetic profiles

The shape of anomaly 25r differs from one location to the next because it depends on the remanent inclination and declination, the azimuth of the magnetic anomaly lineation, and the inclination and declination of the present geomagnetic field, all of which vary over the Pacific plate. The first step in a palaeomagnetic analysis of marine magnetic anomalies is to describe the skewness of an anomaly by a phase parameter $\Delta\theta$. We take $\Delta\theta$ to be the phase shift that gives an observed anomaly a shape most similar to that expected for sea-floor formed and observed in a downward vertical magnetic field. We estimate $\Delta\theta$ by finding the best visual match between a phase-shifted observed anomaly and an ideal zero-phase-shift synthetic magnetic anomaly (e.g. see Fig. 1). The criteria used to decide what value of $\Delta\theta$ is best are mainly that the shape of the anomaly should match the square-wave like appearance of the synthetic, and that the slope of the main central portion of the anomaly (in this case the slope of the base as we are dealing with a reversed chron) should match the slope of the synthetic. If these criteria are in conflict, we choose the phase shift that makes the base of 25r most closely approach the slope of the synthetic, which is nearly horizontal. For all profiles the phase shift is estimated to the nearest degree.

The synthetics are calculated assuming a downward vertical magnetization of the sea-floor, a downward vertical ambient field, and a 0.5 km thick vertically magnetized source layer located at 4.5 km below sea-level (Schouten 1971; Schouten & McCamy 1972; Schouten & Cande 1976; Cande 1976). The depth of the top of the magnetic layer is inferred from the observed bathymetry. In calculating the synthetic anomalies, we use a Gaussian transition-width filter, which accounts for the finite interval over which the magnetic layer switches from a predominantly normal polarity to a predominantly reversed polarity or vice versa (Blakely 1976). We found from trial and error that a transition width of 16 km (corresponding to a Gaussian standard deviation of ±4.0 km) matched the observed shapes and relative amplitudes of the anomalies. This is not to say that all aspects of the shapes and relative amplitudes are well matched, but that this range of widths seems to give the best compromise. Spreading rates for the synthetics are calculated from published stage poles and angles or from

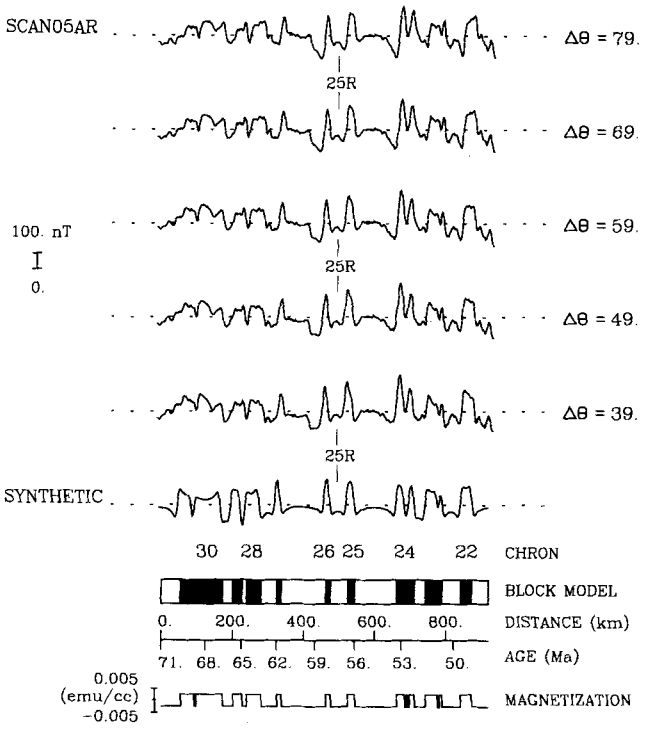


**Figure 1.** Example of deskewing anomaly 25r on a magnetic profile. The profile shown is SCAN05AR, one of the northern profiles recording Pacific–Farallon spreading. The phase shift applied to the magnetic profile is shown on the right side of the profile. The best phase shift for deskewing anomaly 25r on this profile was chosen at 59°. The base of anomaly 25r tilts up towards anomaly 25 for phase shifts smaller than 59°, and tilts up towards anomaly 26 for phase shifts larger than 59°. The anomaly amplitude scale is shown on the left side of the figure. A synthetic profile, along with the block model and magnetization used to generate it, is shown under the profiles for comparison. The ages along the synthetic are based on the time-scale of Cande & Kent (1992), which is used throughout this paper.

differences between published finite rotations (Engebretson, Cox & Gordon 1984; Stock & Molnar 1982, 1987).

The *apparent* effective remanent inclination of the sea-floor is estimated from an experimentally determined phase shift $\Delta\theta$ by

$$e_a = -\Delta\theta - e + 180° \tag{1}$$

(Schouten 1971; Schouten & McCamy 1972; Schouten & Cande 1976; Petronotis *et al.* 1992), where $e$, the ambient effective inclination at the site, is obtained from

$$e = \tan^{-1}\left(\frac{\tan I}{\sin \alpha}\right), \tag{2}$$

$$\alpha = A - D. \tag{3}$$

$I$ and $D$ are the inclination and declination of the ambient geomagnetic field at the site estimated from the International Geomagnetic Reference Field. $A$, the azimuth of the magnetic lineation at the site, is taken to be the strike direction that is 90° clockwise from the direction in which the sea-floor becomes younger.

Most prior studies have referred to $e_a$ as the effective remanent inclination. In hindsight, this is true only if anomalous skewness is negligible. The apparent effective remanent inclination may differ from the true effective remanent inclination for several reasons including tectonic rotation of the oceanic crust about a horizontal ridge-parallel axis (Cande 1976; Verosub & Moores 1981), variations in the intensity of the geomagnetic field within the same polarity interval (Cande 1978), chemical remagnetization of the oceanic crust (Raymond & LaBrecque 1987), and the occurrence of non-vertical boundaries between blocks of sea-floor with alternating polarity, as expected if magnetized lower crust and upper mantle contribute significantly to the observed anomaly (Blakely 1976; Cande 1978; Arkani-Hamed 1988, 1990). Hence, we draw a distinction between the apparent effective remanent inclination, which can be simply calculated from the observables, and the true effective remanent inclination, which differs from the apparent effective remanent inclination exactly by the anomalous skewness (Petronotis *et al.* 1992).

## Model description

Let **p** be an ordered triple with components $\lambda_p$ (pole latitude), $\phi_p$ (pole longitude), and $\theta_a$ (anomalous skewness). The effective remanent inclination $e_r$ can be predicted by a function that depends on $\lambda_i$ and $\phi_i$ (the coordinates of the site), $\lambda_p$ and $\phi_p$ (the coordinates of the pole), and $A$ (the azimuth of the magnetic lineation):

$$e_r = \tan^{-1}\left(\frac{\tan I_r}{\sin \alpha_r}\right), \tag{4}$$

where

$$\alpha_r = A - D_r, \tag{5}$$

$$I_r = \tan^{-1}\left(2\frac{g_i}{(1-g_i^2)^{1/2}}\right), \qquad -90° \le I_r \le 90°, \tag{6}$$

and

$$D_r = -\tan^{-1}\left(\frac{\cos\lambda_p \sin(\phi_i - \phi_p)}{-\sin\lambda_i \cos\lambda_p \cos(\phi_i - \phi_p) + \cos\lambda_i \sin\lambda_p}\right), \qquad -180° < D_r \le 180°. \tag{7}$$

The cosine of the palaeocolatitude at site $i$, is given by

$$g_i = \cos\lambda_p \cos\lambda_i \cos(\phi_p - \phi_i) + \sin\lambda_p \sin\lambda_i. \tag{8}$$

Given a trial value for anomalous skewness and a trial pole position, a model apparent effective inclination can be predicted at each site

$$e_m = e_r - \theta_a, \tag{9}$$

which can be compared with the observations.

This formulation neglects the possible dependence of anomalous skewness, $\theta_a$, on spreading rate, lineation azimuth, depth or thickness of the magnetic layer, or other factors that may vary from location to location. It may eventually be necessary to correct for predictable dependencies, especially that on spreading rate (Cande 1978; Roest, Arkani-Hamed & Verhoef 1992). Here we mainly neglect these dependencies. Further below, however, we examine the dependence on spreading rate of the residuals in the least-squares fit, and also examine the sensitivity of

the results to an empirical correction for spreading-rate dependence.

The method for finding the least-squares best-fit estimates of pole latitude, pole longitude and anomalous skewness, as well as the method for estimating the information contribution ('importance') of each datum, are described by Petronotis *et al.* (1992).

### Statistical significance of adding anomalous skewness as an adjustable parameter

An $F$-ratio test provides a convenient method for testing the significance of including anomalous skewness as an adjustable parameter along with pole latitude and pole longitude. To make this test we calculate the statistic $F$, where

$$F = \frac{[\chi^2]_{\theta=0} - \chi^2(\theta_{\min})}{\chi^2(\theta_{\min})/(N-3)}, \quad (10)$$

where $[\chi^2]_{\theta=0}$ is the lowest value of chi-square with anomalous skewness fixed at the value of zero, $\chi^2(\theta_{\min})$ is the lowest value of chi-square when anomalous skewness is allowed to adjust, and $N$ is the number of data. If the errors in the data are correctly estimated, if the errors are Gaussian distributed, and if effective inclinations depend linearly on each of the adjustable parameters, $F$ would be $F$ distributed with 1 versus $N-3$ degrees of freedom. Each of these assumptions is questionable in detail, but this test still provides a practical means for quantifying the improvement to the fit by the addition of this one parameter.

### Confidence limits

Confidence limits on the best-fitting pole and anomalous skewness are calculated by two methods, constant-chi-square boundaries and linear propagation of errors. The former method is exact but tedious to compute and describe, whereas the latter can be simply and rapidly calculated and compactly described, but is appropriate only when the linear approximation is accurate. Petronotis *et al.* (1992) explain how to calculate both types of limits, both of which propagate the errors assigned to individual skewness estimates into the error of the pole latitude, of the pole longitude, and of anomalous skewness. Our main reason for calculating both here is that the comparison of the limits from the two different methods provides a test of the accuracy of the linear approximation. If the two confidence limits are similar, the linear approximation is accurate; if they are dissimilar, the linear approximation is inaccurate.

In our past studies, errors were assigned subjectively to the skewness estimates. Such an approach has the obvious drawback that these errors are poorly understood. Herein we analyse enough anomaly crossings for it to be possible to estimate the errors accurately from the dispersion in the data. From a set of skewness estimates with each given unit weight, we find the best-fitting pole and anomalous skewness, and we estimate the standard deviation. This estimated standard deviation is then used as the assigned error that is propagated to estimate the error of each of the three adjustable parameters (i.e. anomalous skewness and pole latitude and longitude).

We group the data in two ways when estimating standard deviations. First, we give each datum unit weight. This approach is the simplest, but has the drawback that the data are obviously of unequal quality. Noise or ambiguities may be caused by rough sea-floor topography, magnetic storms that occurred during the collection of the data, propagating rifts, the proximity of fracture zones, data gaps, and other sources of error. Profiles from ~5°S to 20°N have lower amplitudes and on average probably have lower signal-to-noise ratios than do profiles from other latitudes. Profiles on which the anomaly crossing poorly resembles that on other profiles regardless of the applied value of $\Delta\theta$ are much more uncertain than profiles that can be deskewed into a more typical appearance. Skewnesses estimated from digital profile records from the National Geophysical Data Center (NGDC) archives are more precise than from profiles we had to digitize from figures published in papers. Therefore, our second approach is to assign each datum to a quality group of A, B, C or D with A being the best and D being the worst. There is also an implicit category F—those profiles that are rejected. We try to rate the quality of the crossings as objectively as possible, for example, all profiles digitized from published figures were placed in category D, but some subjectivity is unavoidable.

The standard deviation of each of these groups is separately estimated by finding a best-fitting pole and anomalous skewness for each. The resulting standard deviations are assigned to every datum within a group, and the final pole is computed by combining all data, each being assigned the error objectively estimated for its group.

When errors are estimated from the dispersion of the data, additional uncertainty is introduced into the pole positions due to the uncertainty in the estimates of the errors. This difference corresponds to the difference between estimating confidence limits assuming an $F$-ratio distribution and those found assuming a chi-square distribution, as we assume here. The size of this effect is less than 2 per cent and we neglect it.

Confidence limits are further checked through the use of Monte Carlo simulations. Each simulated datum is constructed by drawing a pseudo-random number from a zero-mean Gaussian distribution with the same standard error as that assigned to the datum. This random number is added to the model effective inclination calculated from the best-fitting pole from the real data. This procedure is repeated for every datum in the real data set until a full set of simulated data is constructed. These simulated data are then inverted using the same least-squares algorithm that is applied to the real data, and a best-fitting pole and anomalous skewness are obtained. This entire procedure is repeated until 10 000 simulated data sets are constructed and their 10 000 best-fitting poles and anomalous skewnesses are found.

## DATA AND SKEWNESS ESTIMATES

We analysed 119 crossings of anomaly 25r on profiles obtained from the NGDC, 20 crossings on profiles obtained from the Lamont-Doherty Geobase data base, and 10 crossings on profiles digitized from enlarged versions of figures published by Christoffel & Falconer (1972) and Kruse (1988). Of these 149 crossings, 17 were too poor to use (Fig. 2). In our final pole analysis we used 132 profiles:

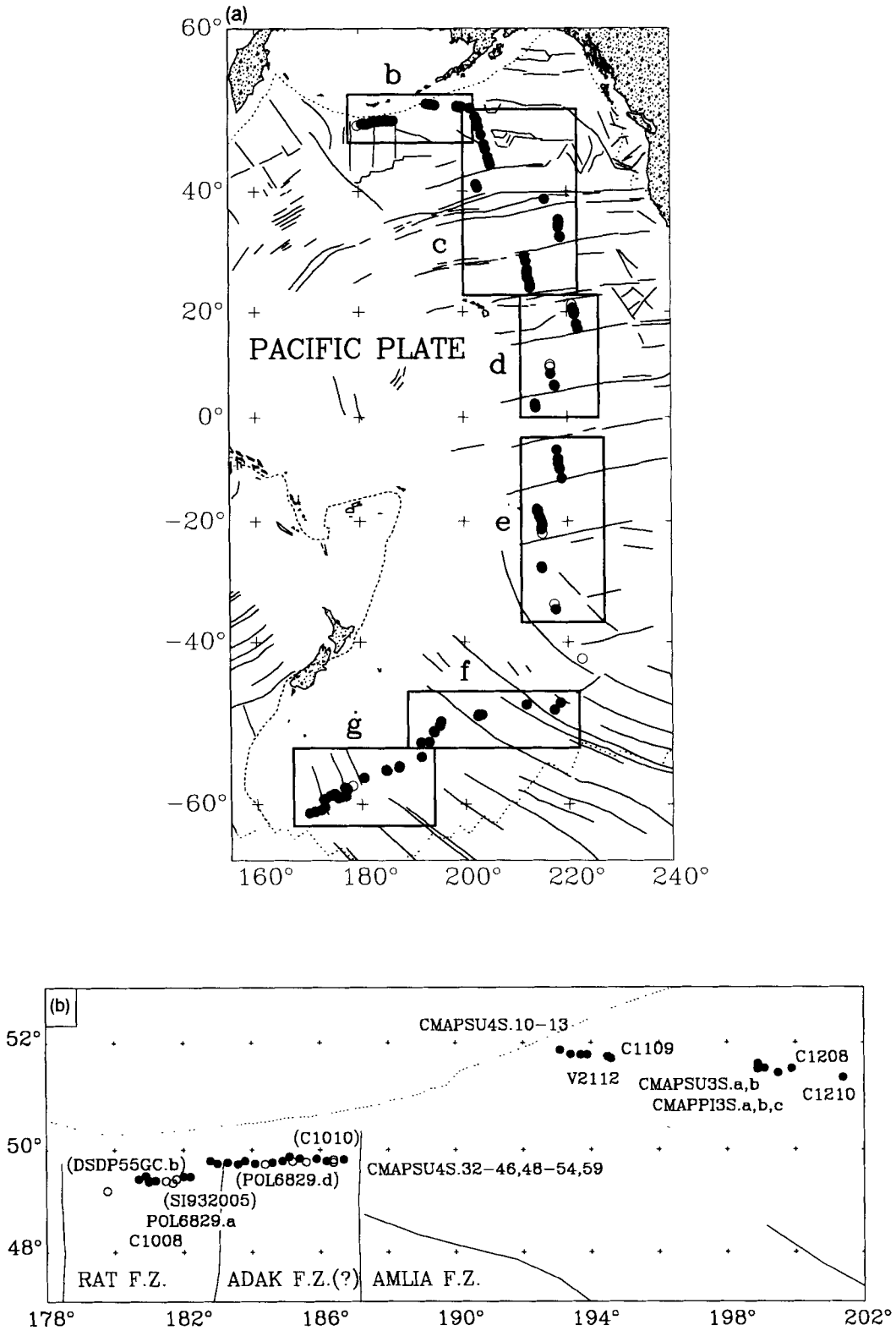


**Figure 2.** Map of the Pacific basin showing locations of crossings of anomaly 25r that are analysed herein. Solid circles show the locations of crossings that were used in determining the preferred pole and open circles show crossings that were excluded. Thin lines show the locations of fracture zones and dotted lines show boundaries, mainly outlining the Pacific plate. Six subregions of the Pacific plate are shown in more detail in: (b) Pacific–Kula crossings; (c) northern Pacific–Farallon crossings; (d) central Pacific–Farallon crossings; (e) southern Pacific–Farallon crossings; (f) Pacific–Bellingshausen crossings; (g) Pacific–Antarctic crossings. In each part we have labelled all the crossings analysed and the major fracture zones mentioned in the discussion. (Mercator projections.)

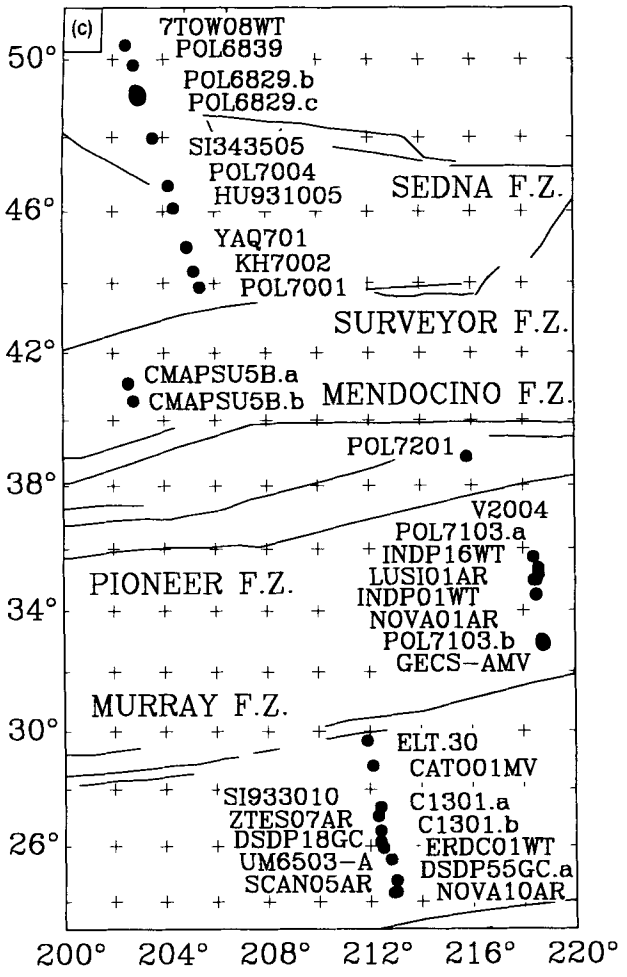


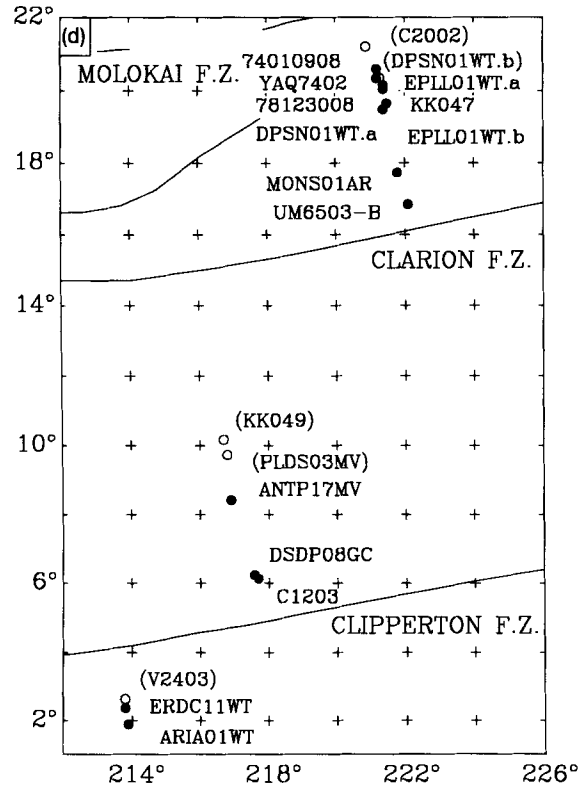


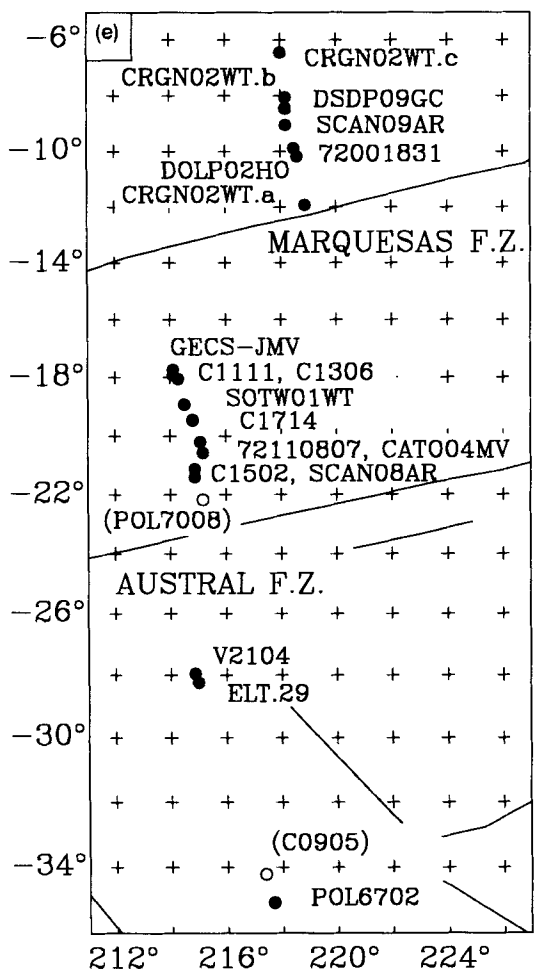


**Figure 2.** (*Continued.*)

33 recording Pacific–Kula spreading (Fig. 3), 66 recording Pacific–Farallon spreading (Figs 4, 5 and 6), 12 recording Pacific–Bellingshausen spreading (Fig. 7), and 21 recording Pacific–Antarctic spreading (Fig. 8). Of these 132 skewness estimates, 16 were assigned to category A, 44 to category B, 29 to category C, and 43 to category D. The locations of these profiles are listed in Table 1 and shown in Fig. 2 with solid circles. The original and deskewed shapes of the profiles excluded from the preferred pole are shown in Fig. 9, and their locations are shown in Fig. 2 with open circles.

### Pacific–Kula crossings

We analysed 42 crossings of anomaly 25r over sea-floor formed by Pacific–Kula spreading (Fig. 2b), 33 of which were used in the final pole analysis. All the rejected crossings are located east of the Rat and west of the Amlia fracture zones (Fig. 2b) where the anomaly crossings are complicated by small offsets of the anomaly pattern (Hayes & Heirtzler 1968; Grim & Erickson 1969; Lonsdale 1988, Atwater & Severinghaus 1989). Of the 33 retained crossings, 20 are located between the Rat and Amlia fracture zones, six lie east of Amlia fracture zone, near the intersection of anomaly 25r with the Aleutian trench, and the seven easternmost crossings are near the Great Magnetic

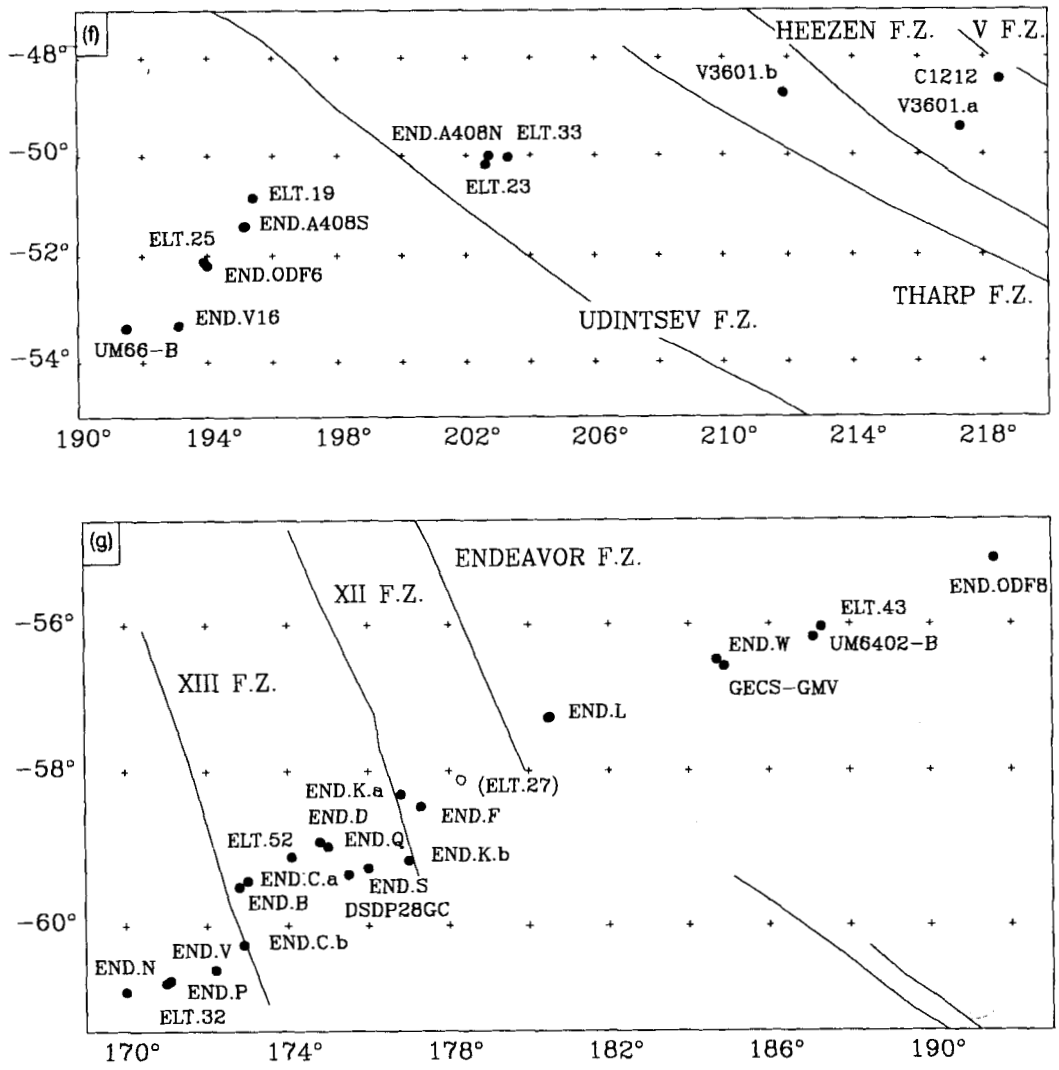


**Figure 2.** (*Continued.*)

Bight (Fig. 2b). The Pacific–Kula anomalies have moderate amplitudes (300–500 nT peak to trough) west of the Amlia fracture zone and high amplitudes (600–1000 nT peak to trough) east of the Amlia fracture zone (Fig. 3). The half-rates we estimate for these profiles by comparing the anomaly 25 to 27 sequence with synthetic magnetic-anomaly profiles range from 17 to 23 mm $yr^{-1}$; these rates are similar to, or slightly faster than, the 16–17 mm $yr^{-1}$ predicted from the anomaly 27–25 stage pole and angular rate of Engebretson *et al.* (1984) and similar to, or sightly slower than, the 23–24 mm $yr^{-1}$ predicted by the anomaly 30/31–25 stage pole and angle of Rosa & Molnar (1988).

Most of the westernmost profiles were collected during the Seamap survey of 1964 and consist of closely spaced parallel N–S tracks that cross the Aleutian trench (Grim & Erickson 1969). Despite the closeness of the profiles, however, the shapes and skewnesses of anomaly 25r are not as consistent from crossing to crossing as one would expect. One reason for this is the roughness of the sea-floor. Whereas the sea-floor east of the Amlia fracture zone is smooth, the sea-floor west of the fracture zone is dominated by closely spaced E–W trending ridges and troughs with a relief of ~500 m (Grim & Erickson 1969). These ridges can be seen in the bathymetric data of individual profiles and can be traced from one profile to the next. Another complication is the presence of several small oblique offsets that disrupt the sequence and spacing of the anomalies. One such offset, identified by Lonsdale (1988) as the Amchitka fracture zone, does affect the shape of profile DSDP55GC.a, and may affect profiles C1008, POL6829.a, CMAPSU4S.53 and CMAPSU4S.54. Wherever possible, we used the anomaly identifications of Grim & Erickson (1969), Lonsdale (1988), and Atwater & Severinghaus (1989) to compare with our own correlations. These agreed in nearly all cases.

The estimation of the skewness of each of these anomaly crossings is straightforward for the profiles located east of the Amlia fracture zone, with estimates of $\Delta\theta$ ranging from 65° to 118° (Fig. 3). Four of these were assigned to error category A, seven to category B, one to category C, and one to category D. The estimation of the skewness of the crossings located west of Amlia fracture zone is more complicated for the reasons discussed above. The skewness estimates of these profiles range from 10° to 117° (Fig. 3).

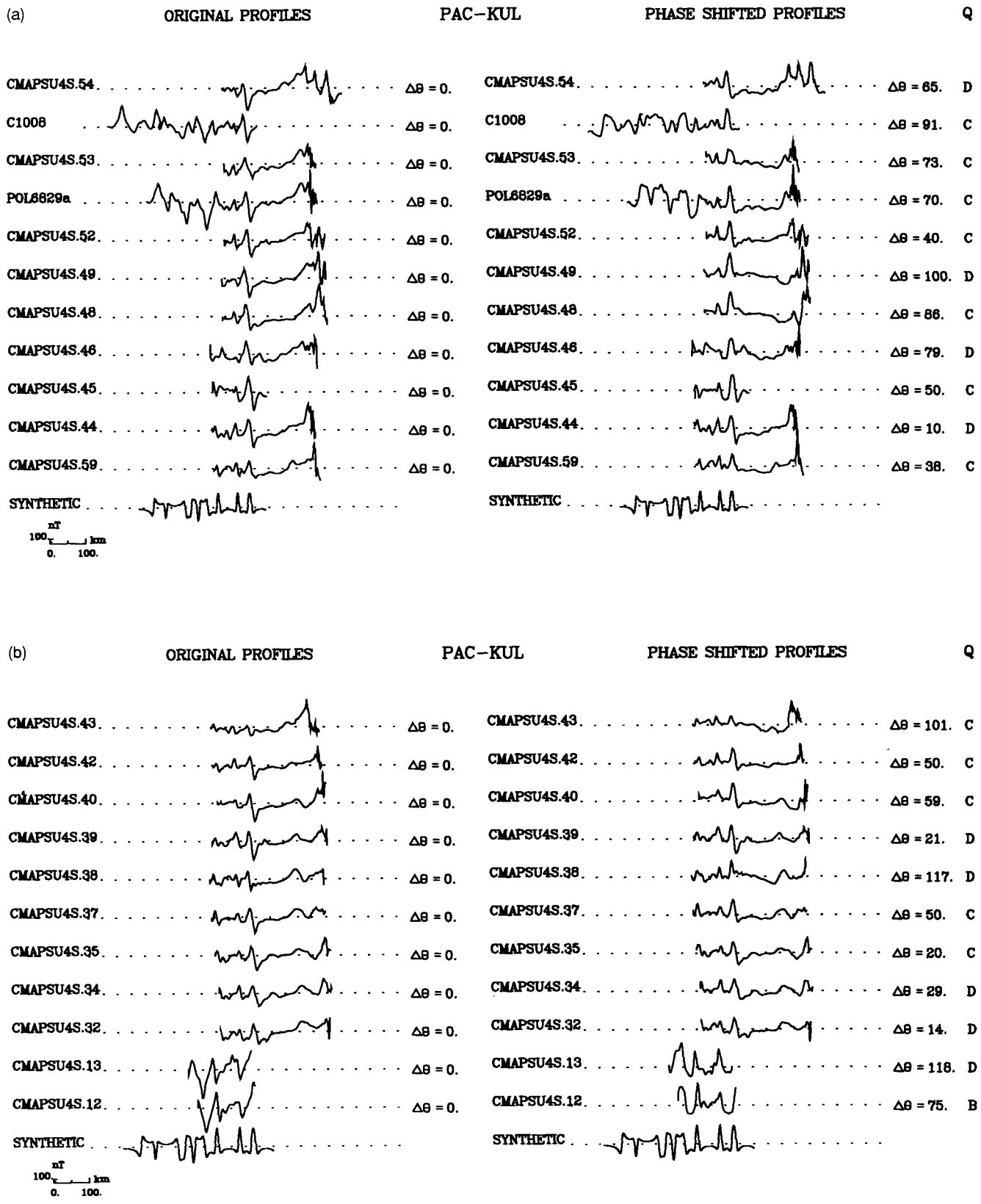


**Figure 3.** Profiles obtained over sea-floor produced by Pacific–Kula sea-floor spreading. Original profiles projected perpendicular to lineation strike are shown on the left and phase-shifted profiles are on the right. The phase shift ($\Delta\theta$) that best deskews anomaly 25r and the quality ($Q$) of the anomaly is shown on the right side of the deskewed profile. The synthetic profiles show the sequence from (normal) anomaly 31 (on the left) to (normal) anomaly 25 (on the right). The east longitude of the profiles increases from the top to the bottom of the figure. The high-amplitude positive anomaly on the right side of profiles CMAPSU4S.54 through CMAPSU4S.32 is the signature of the Aleutian arc.

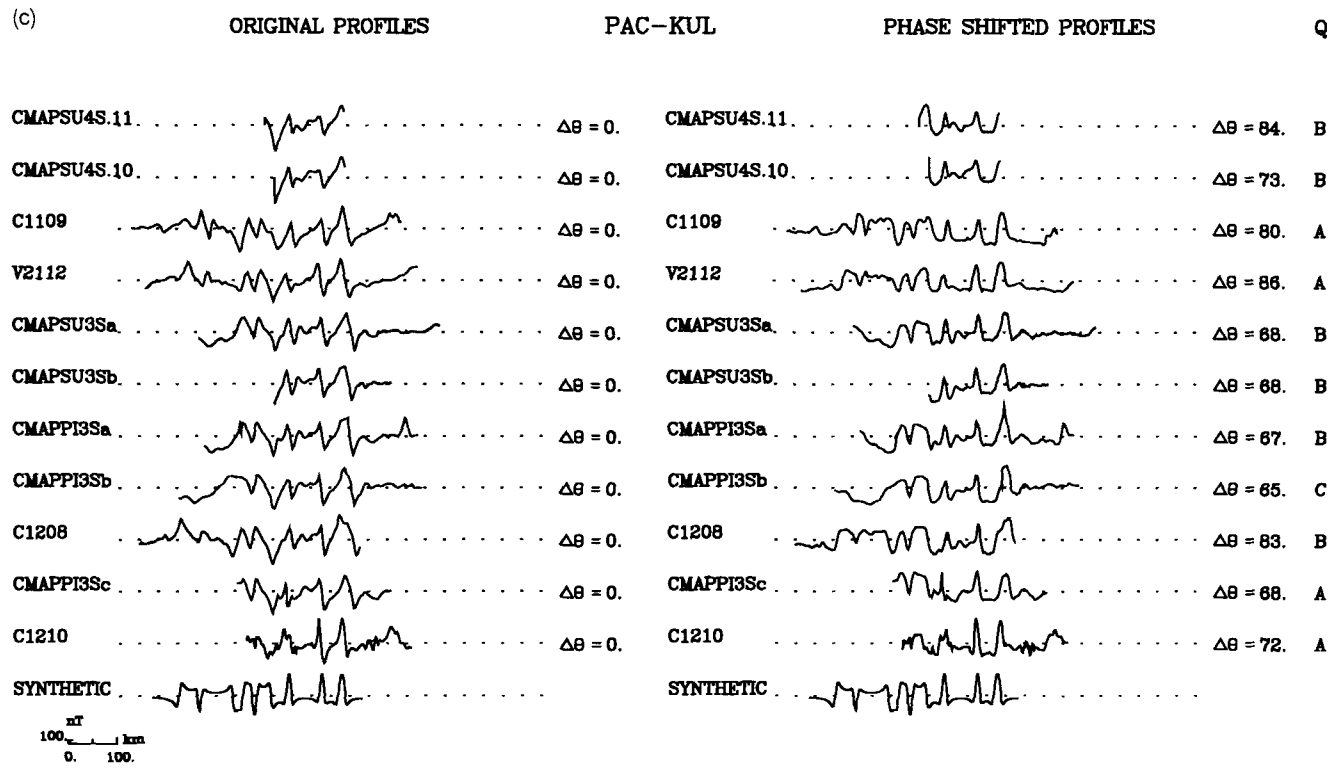


**Figure 3.** (*Continued.*)

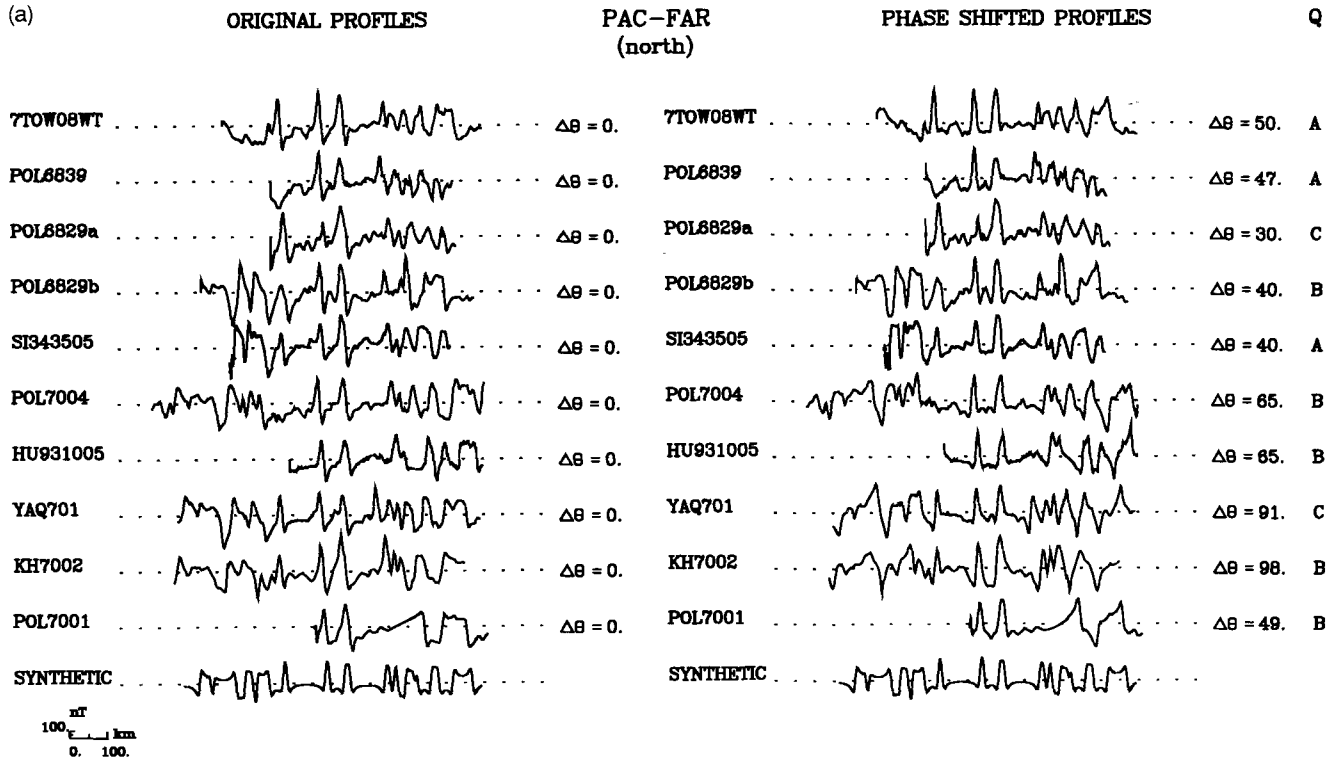


**Figure 4.** Profiles obtained over the sea-floor between 52° and 22°N produced by Pacific–Farallon sea-floor spreading. The north latitude of the profiles decreases from the top to the bottom of the figure. The synthetic profiles show the sequence from (normal) anomaly 31 (on the left) to (normal) anomaly 21 (on the right) on parts (a) and (b) and from anomaly 31 to (normal) anomaly 22 on part (c).

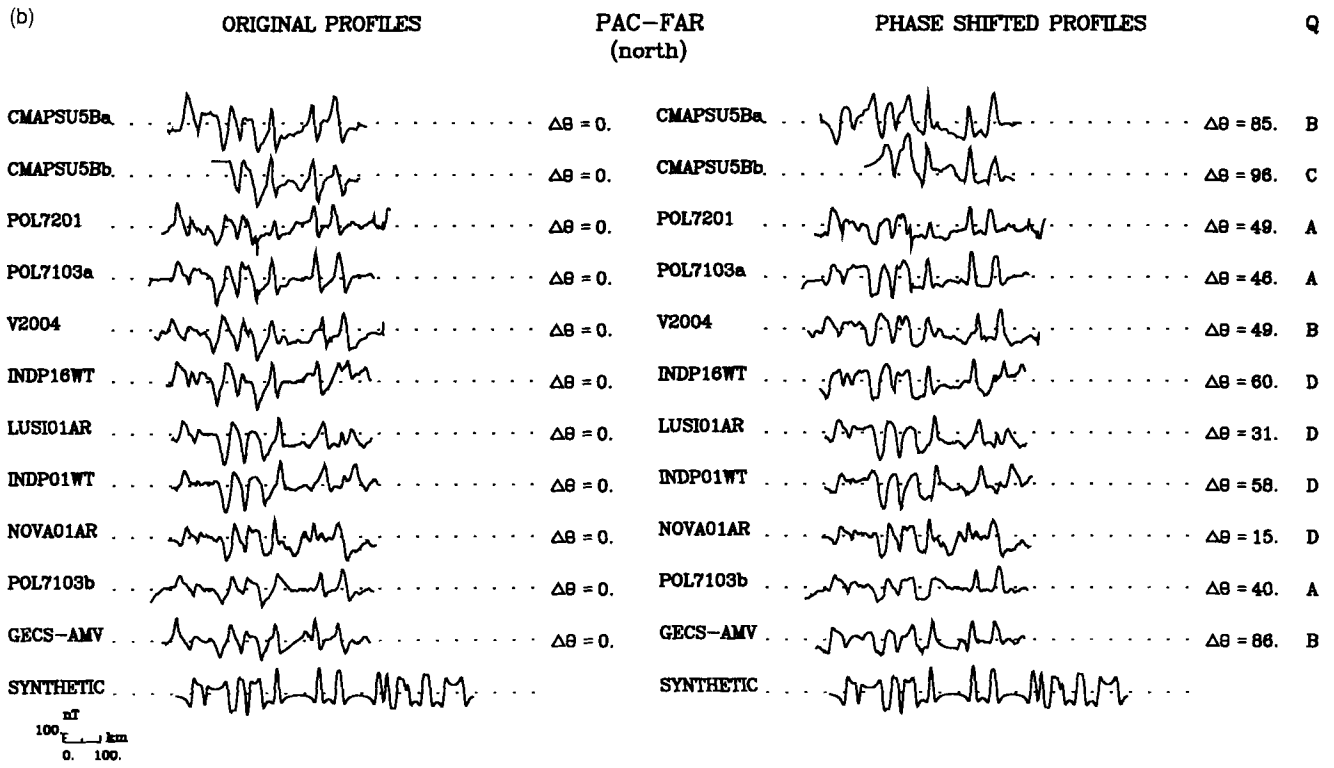


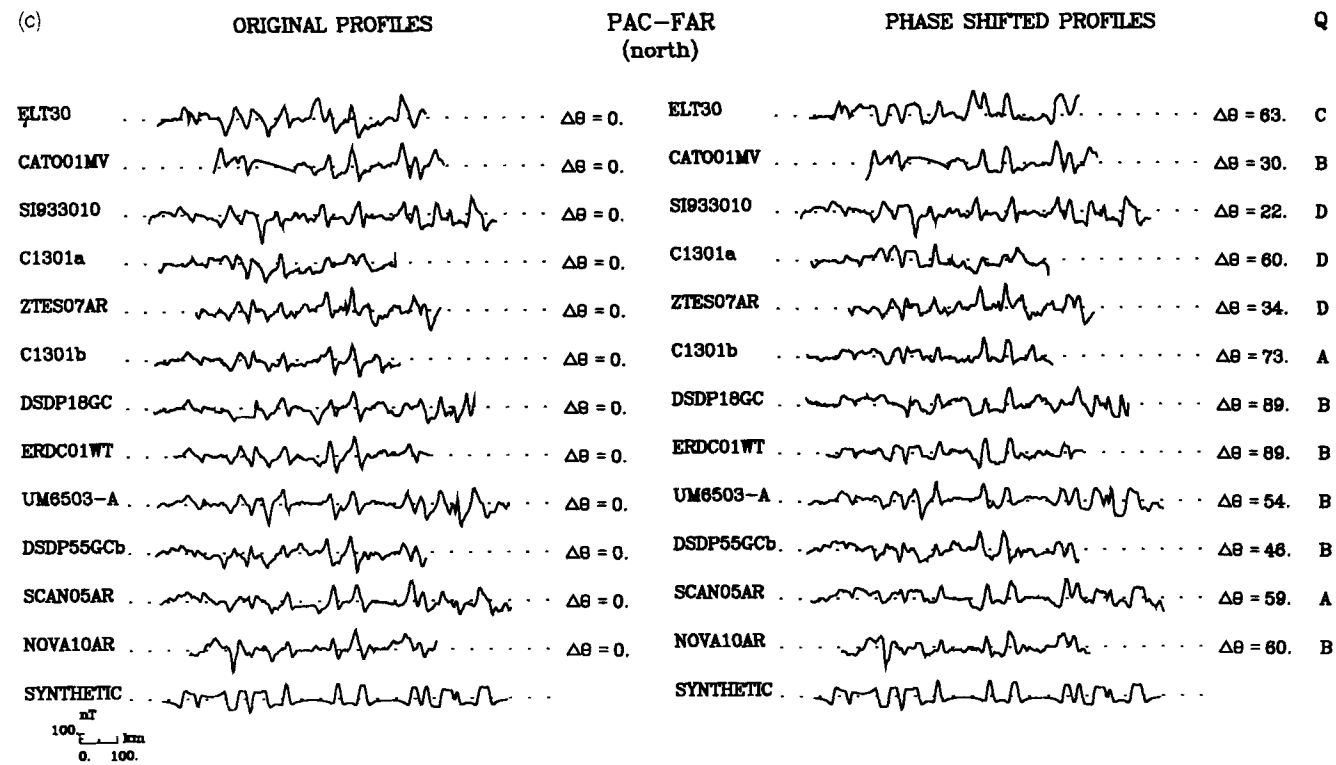


**Figure 4.** (*Continued.*)

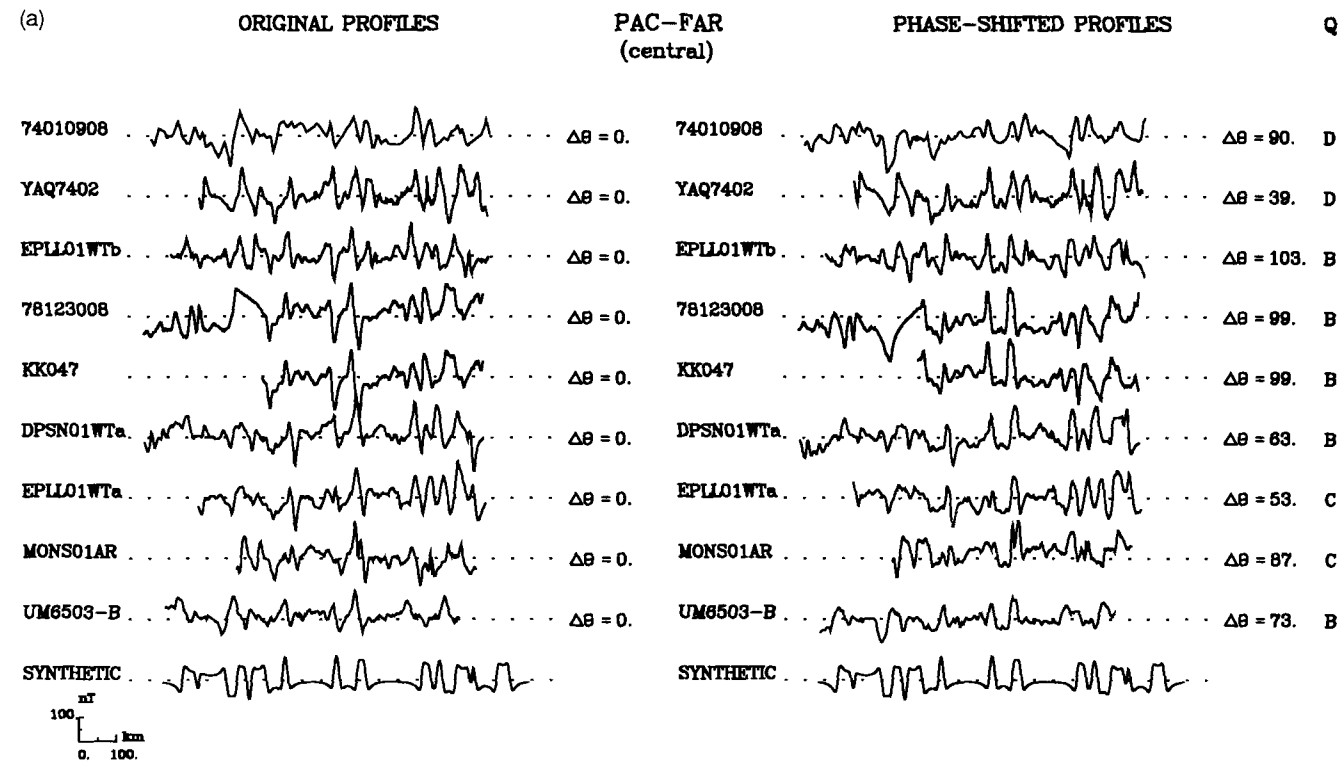


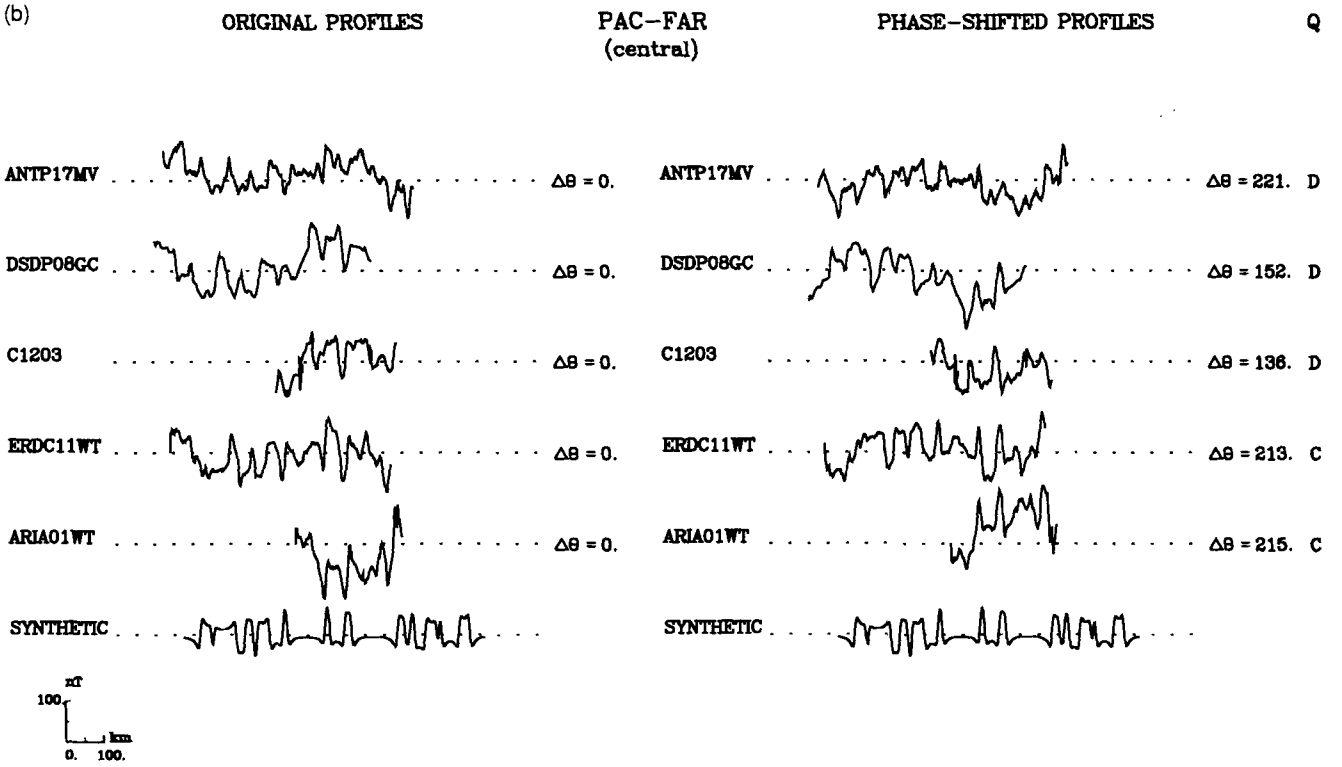


**Figure 5.** Profiles obtained over sea-floor between 22°N and the equator produced by Pacific–Farallon sea-floor spreading. The north latitude of the profiles decreases from the top to the bottom of the figure. The synthetic profiles show the sequence from (normal) anomaly 31 (on the left) to (normal) anomaly 22 (on the right).

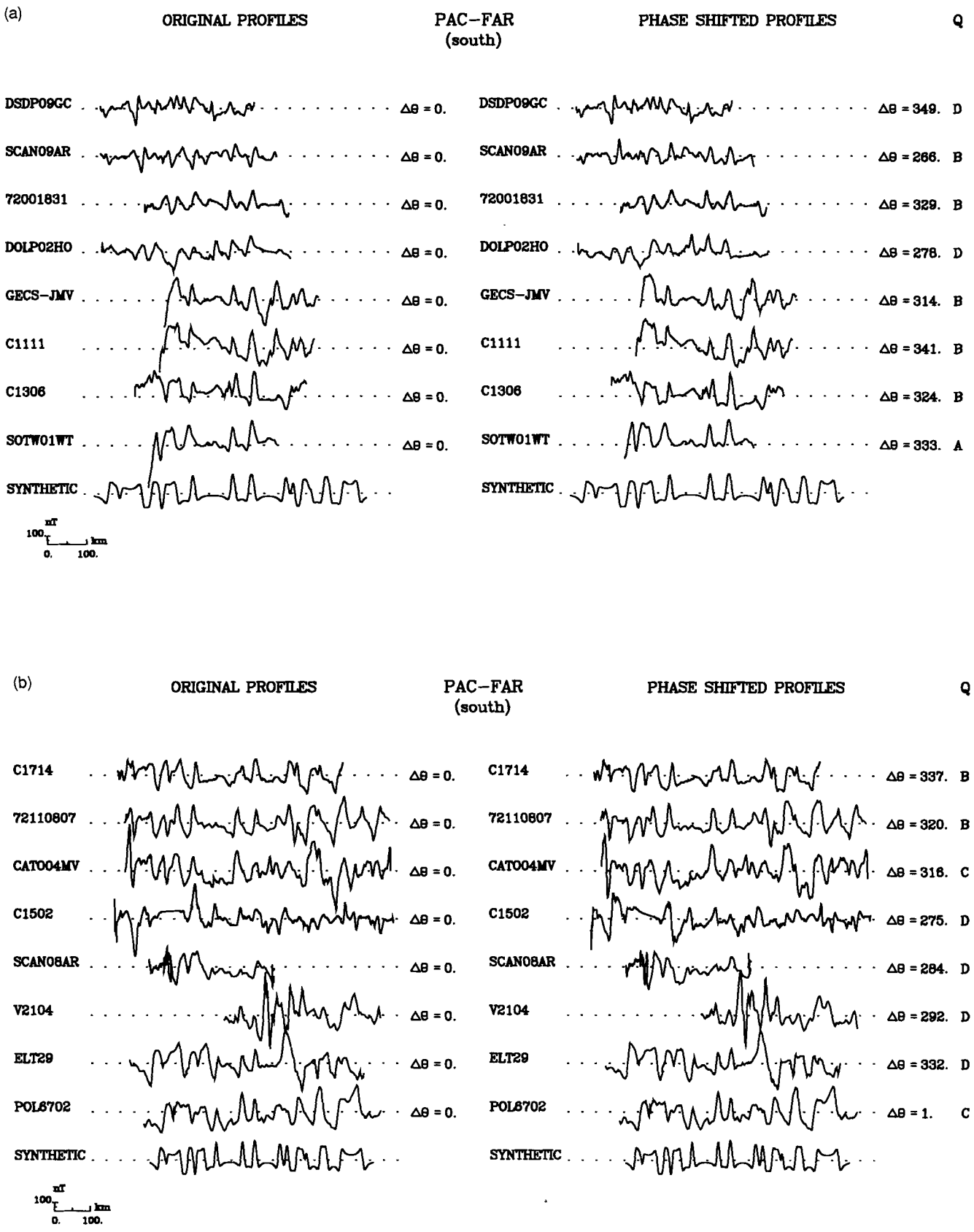


**Figure 6.** Profiles obtained over sea-floor between 6°S and 35°S produced by Pacific–Farallon sea-floor spreading. The south latitude of the profiles increases from the top to the bottom of the figure. The synthetic profiles show the sequence from (normal) anomaly 31 (on the left) to (normal) anomaly 21 (on the right).

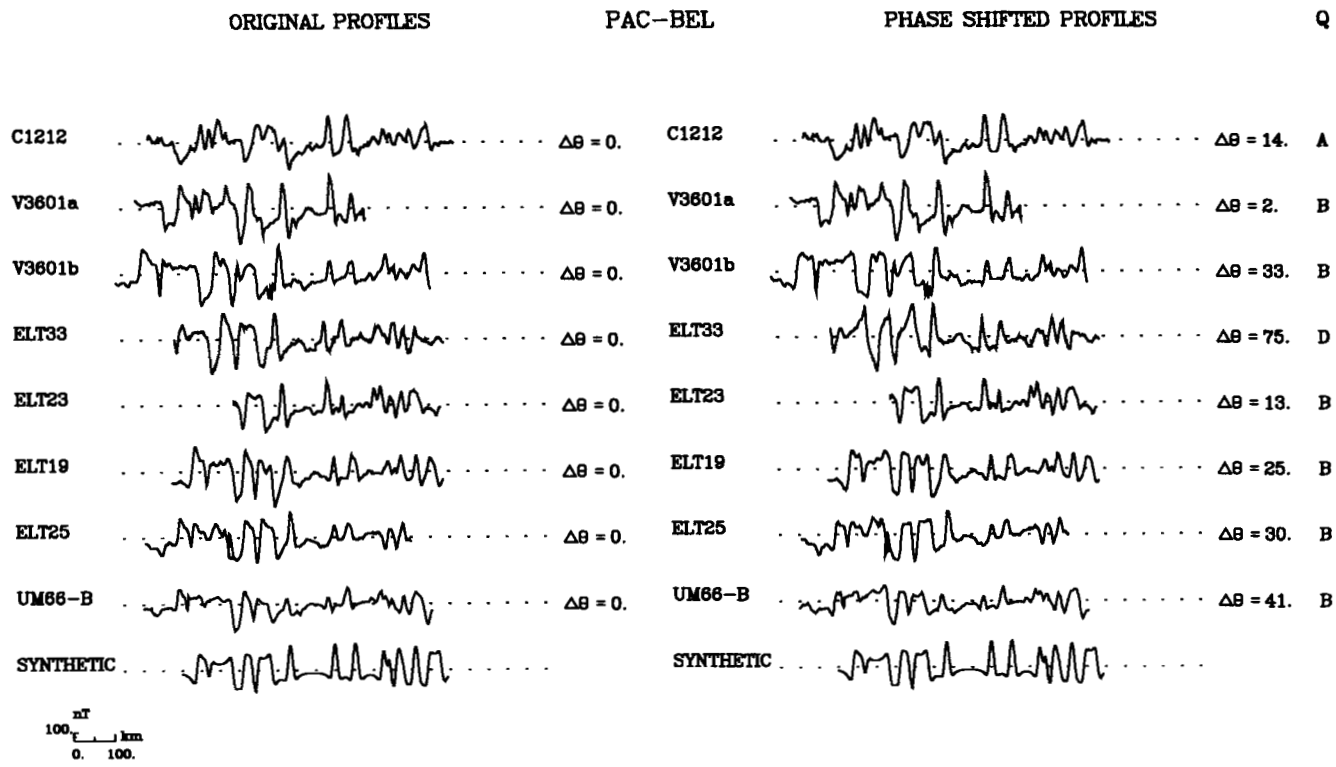


**Figure 7.** Profiles obtained over sea-floor produced by Pacific–Bellingshausen sea-floor spreading. The east longitude of the profiles decreases from the top to the bottom of the figure. The synthetic profiles show the sequence from (normal) anomaly 31 (on the left) to (normal) anomaly 21 (on the right).

Twelve profiles were assigned to error category C and eight to error category D.

### Pacific–Farallon crossings

It is convenient to divide these into three groups: northern (north of 22°N), central (between the equator and 22°N), and southern (south of 5°S).

#### *Northern Pacific–Farallon crossings*

The 33 profiles analysed in this group lie south of the Great Magnetic Bight and north of the Molokai fracture zone (Fig. 2c). These profiles typically have peak-to-trough amplitudes that range from 600 nT in the north to 200 nT in the south (Fig. 4). The spreading rate is predicted to be 37–43 mm $yr^{-1}$ by the model of Engebretson *et al.* (1984) and 26–32 mm $yr^{-1}$ by the model of Rosa & Molnar (1988), increasing from north to south in both cases. Our best estimates of the half-rates obtained from the anomaly 25 to 27 sequence range from 29 to 33 mm $yr^{-1}$, ~22 per cent slower than the half-rates predicted by the anomaly 34–25 stage pole and angular rate of Engebretson *et al.* (1984) and ~7 per cent faster than the half-rates predicted by the anomaly 30/31–25 stage pole and angle of Rosa & Molnar (1988) (Fig. 10).

The northernmost subgroup of these profiles, south of the Great Magnetic Bight and north of the Surveyor fracture zone, have large amplitudes and are of excellent quality. The only complications are a slightly atypical appearance of anomaly 25r on profiles KH7002 and YAQ701, which were assigned to error category C. Profile YAQ701 also shows an extra peak between anomalies 24 and 25; this feature is correlated with a seamount in the sea-floor topography and appears to have no effect on the shape of anomaly 25. Four of the profiles we used between the Murray and Molokai fracture zones (C1301a, ZTES07AR, C1301b and DSDP18GC; Fig. 4c) show an extra positive anomaly on the young side of anomaly 25. Atwater & Severinghaus (1989, especially see their Plate 3b) have mapped a 'wandering small offset' adjacent to where this extra anomaly occurs on these four profiles, and have interpreted the offset (and other wandering small offsets) as the long-term manifestation of recurrent overlapping spreading centres (Macdonald *et al.* 1988). The extra anomaly seems well-enough separated from the anomaly 25–26 sequence on C1301b and DSDP18GC to have little effect on the interpretation of the skewness, and we have assigned them to category A and B, respectively. However, it affects the shape of anomaly 25 on C1301a and ZTES07AR; these poorer quality profiles were both assigned to category D. The same offset results in the width of anomaly 25r being sightly larger on profile SI933010 and for that reason it was also included in category D. Another group of profiles between the Pioneer and Murray fracture zones (INDP16WT, LUSI01AR, INDP01WT and NOVA01AR; Fig. 4b) seem to be similarly affected by another 'wandering small offset'; because of their poor quality they were also assigned to category D. The first three of these profiles, along with V2004, the next profile to the north, give spreading rates that are 16 per cent faster than the average 31 mm $yr^{-1}$ obtained from the remaining profiles.

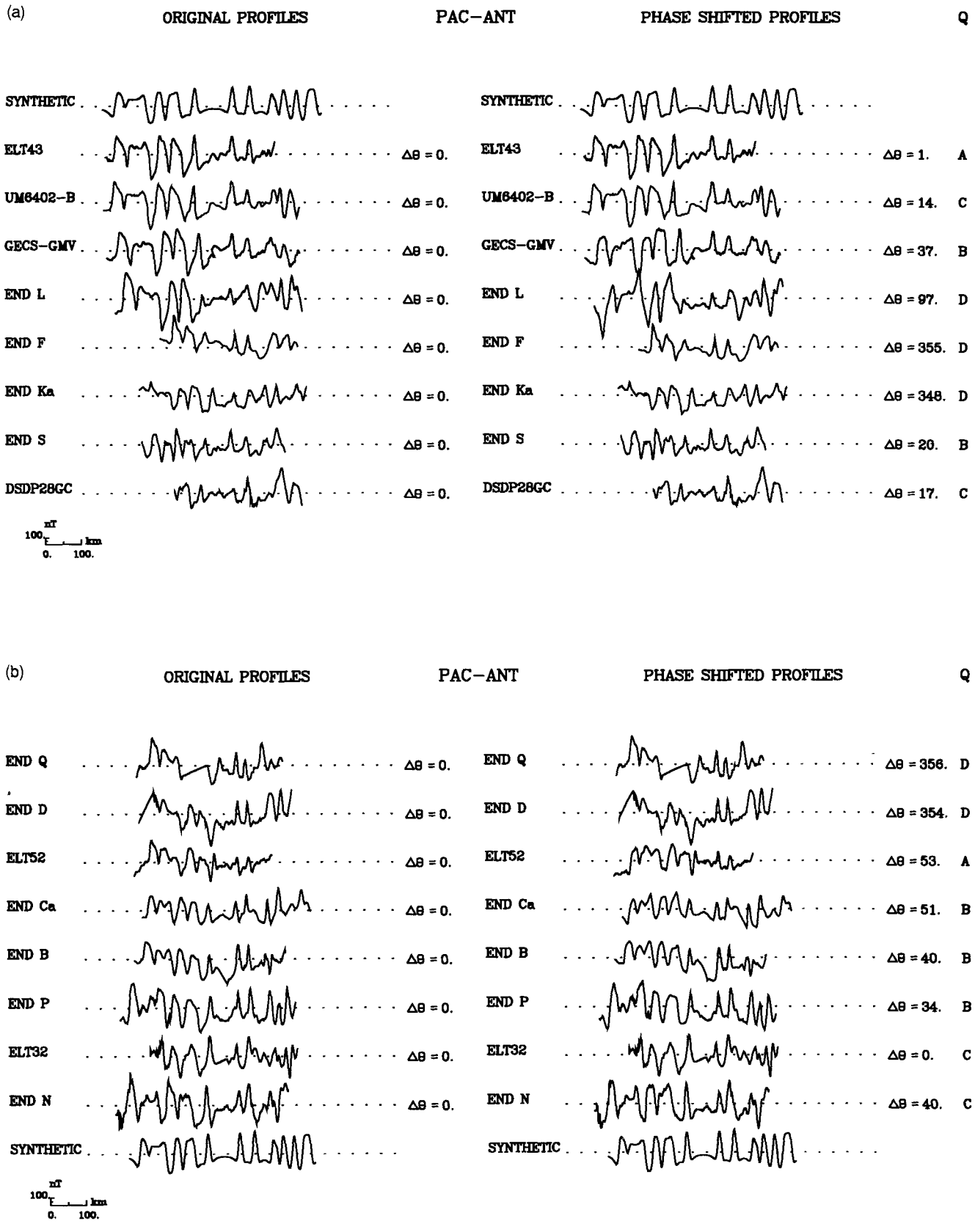


**Figure 8.** Profiles obtained over sea-floor produced by Pacific–Antarctic sea-floor spreading. The east longitude of the profiles decreases from the top to the bottom of the figure. The synthetic profiles in parts (a) (top) and (b) (bottom) show the sequence from (normal) anomaly 31 (on the left) to (normal) anomaly 21 (on the right).

**Table 1.** Chron 25r pole (56.5–57.8 Ma).

Pole Location: 78.2° N, 4.8° E, Anomalous Skewness = 16.2° ± 4.6°

| 95% Confidence Ellipse | | | Error Covariance Matrix | | |
|---|---|---|---|---|---|
| Semi Axis | Length of Semiaxis | Orientation (cw from N) | 2.777 | -0.206 | 2.323 |
| Major | 6.4° | 93.0 | -0.206 | 6.741 | -0.983 |
| Minor | 4.1° | 183.0 | 2.323 | -0.983 | 5.420 |

$\chi^2$ = 128.65 with 129 degrees of freedom

| Profile | Lat (°N) | Long (°E) | Δθ(°) | Azim (°) | Datum $e_a$(°) | $\sigma_\theta$(°) | Model $e_m$(°) | Residual(°) | Importance |
|---|---|---|---|---|---|---|---|---|---|
| *Seafloor Created by Pacific - Kula Spreading* | | | | | | | | | |
| *East of Rat F.Z. and West of Amlia F.Z.* | | | | | | | | | |
| cmapsu4s.54 * | 49.4 | 180.7 | 65.0 | 87.0 | 53.9 | 39.6 | 40.9 | 12.9 | 0.002 |
| c1008 | 49.5 | 180.9 | 91.0 | 87.0 | 27.8 | 24.9 | 41.0 | -13.2 | 0.006 |
| cmapsu4s.53 | 49.4 | 181.0 | 73.0 | 87.0 | 45.9 | 24.9 | 40.9 | 5.0 | 0.006 |
| pol6829.a | 49.4 | 181.0 | 70.0 | 87.0 | 49.0 | 24.9 | 40.9 | 8.1 | 0.006 |
| cmapsu4s.52 | 49.4 | 181.2 | 40.0 | 87.0 | 78.8 | 24.9 | 40.9 | 37.9 | 0.006 |
| cmapsu4s.49(B) | 49.5 | 182.0 | 100.0 | 88.0 | 18.7 | 39.6 | 40.9 | -22.2 | 0.002 |
| cmapsu4s.48(C) | 49.5 | 182.2 | 86.0 | 88.0 | 32.7 | 24.9 | 40.9 | -8.2 | 0.006 |
| cmapsu4s.46(E) | 49.8 | 182.8 | 79.0 | 88.0 | 39.4 | 39.6 | 41.2 | -1.9 | 0.002 |
| cmapsu4s.45(F) | 49.7 | 183.0 | 50.0 | 88.0 | 68.4 | 24.9 | 41.2 | 27.2 | 0.006 |
| cmapsu4s.44(G) | 49.8 | 183.3 | 10.0 | 89.0 | 108.4 | 39.6 | 41.2 | 67.2 | 0.002 |
| cmapsu4s.59 | 49.7 | 183.6 | 38.0 | 89.0 | 80.4 | 24.9 | 41.2 | 39.2 | 0.006 |
| cmapsu4s.43 | 49.8 | 183.8 | 101.0 | 89.0 | 17.3 | 24.9 | 41.2 | -23.9 | 0.006 |
| cmapsu4s.42 | 49.7 | 184.1 | 50.0 | 89.0 | 68.3 | 24.9 | 41.2 | 27.1 | 0.006 |
| cmapsu4s.40 | 49.8 | 184.6 | 59.0 | 90.0 | 59.3 | 24.9 | 41.2 | 18.1 | 0.006 |
| cmapsu4s.39 | 49.8 | 184.9 | 21.0 | 90.0 | 97.2 | 39.6 | 41.2 | 56.0 | 0.002 |
| cmapsu4s.38 | 49.9 | 185.1 | 117.0 | 90.0 | 1.1 | 39.6 | 41.3 | -40.2 | 0.002 |
| cmapsu4s.37 | 49.8 | 185.4 | 50.0 | 90.0 | 68.1 | 24.9 | 41.3 | 26.8 | 0.006 |
| cmapsu4s.35 | 49.8 | 185.9 | 20.0 | 91.0 | 98.1 | 24.9 | 41.3 | 56.8 | 0.006 |
| cmapsu4s.34 | 49.8 | 186.2 | 29.0 | 91.0 | 89.1 | 39.6 | 41.2 | 47.9 | 0.002 |
| cmapsu4s.32 | 49.8 | 186.7 | 14.0 | 91.0 | 104.0 | 39.6 | 41.2 | 62.7 | 0.002 |
| *East of Amlia F.Z. and West of the Great Magnetic Bight* | | | | | | | | | |
| cmapsu4s.13(R) | 51.9 | 193.1 | 118.0 | 95.0 | -2.5 | 39.6 | 43.2 | -45.7 | 0.002 |
| cmapsu4s.12(S) | 51.8 | 193.4 | 75.0 | 96.0 | 40.6 | 18.4 | 43.2 | -2.6 | 0.010 |
| cmapsu4s.11(T) | 51.8 | 193.7 | 84.0 | 96.0 | 31.6 | 18.4 | 43.2 | -11.6 | 0.010 |
| cmapsu4s.10(U) | 51.8 | 193.9 | 73.0 | 96.0 | 42.5 | 18.4 | 43.2 | -0.6 | 0.010 |
| c1109 | 51.7 | 194.6 | 80.0 | 96.0 | 35.6 | 13.2 | 43.2 | -7.6 | 0.019 |
| v2112 | 51.7 | 194.6 | 86.0 | 96.0 | 29.5 | 13.2 | 43.1 | -13.7 | 0.019 |
| cmapsu3s.a | 51.5 | 198.9 | 68.0 | 99.0 | 47.1 | 18.4 | 43.1 | 4.0 | 0.010 |
| cmapsu3s.b | 51.5 | 198.9 | 68.0 | 99.0 | 47.1 | 18.4 | 43.2 | 3.9 | 0.010 |
| cmappi3s.a | 51.6 | 198.9 | 67.0 | 100.0 | 48.1 | 18.4 | 43.3 | 4.8 | 0.010 |
| cmappi3s.b | 51.5 | 199.1 | 65.0 | 100.0 | 50.1 | 24.9 | 43.2 | 6.9 | 0.005 |
| c1208 | 51.4 | 199.5 | 83.0 | 100.0 | 32.1 | 18.4 | 43.2 | -11.1 | 0.010 |
| cmappi3s.c | 51.5 | 199.9 | 68.0 | 100.0 | 47.0 | 13.2 | 43.2 | 3.7 | 0.019 |
| c1210 | 51.3 | 201.4 | 72.0 | 101.0 | 42.8 | 13.2 | 43.2 | -0.4 | 0.019 |
| Subtotal | | | | | | | | | 0.241 |
| *Seafloor Created by Pacific - Farallon Spreading (Northern)* | | | | | | | | | |
| *South of the Great Magnetic Bight and North of Surveyor F.Z.* | | | | | | | | | |
| 7tow08wt | 50.4 | 202.5 | 50.0 | 162.0 | 55.8 | 13.2 | 60.5 | -4.8 | 0.038 |
| pol6839 | 49.9 | 202.8 | 47.0 | 162.0 | 59.1 | 13.2 | 60.3 | -1.2 | 0.038 |
| pol6829.b | 49.2 | 202.9 | 30.0 | 162.0 | 76.3 | 24.9 | 60.0 | 16.4 | 0.011 |
| pol6829.c | 49.0 | 203.1 | 40.0 | 162.0 | 66.4 | 18.4 | 59.8 | 6.6 | 0.020 |
| si343505 | 48.0 | 203.6 | 40.0 | 163.0 | 66.4 | 13.2 | 59.9 | 6.5 | 0.039 |
| pol7004 | 46.7 | 204.2 | 65.0 | 163.0 | 41.9 | 18.4 | 59.2 | -17.3 | 0.020 |
| hu931005 | 46.1 | 204.4 | 65.0 | 163.0 | 42.1 | 18.4 | 58.9 | -16.8 | 0.020 |
| yaq701 | 45.0 | 204.9 | 91.0 | 164.0 | 16.2 | 24.9 | 59.0 | -42.8 | 0.011 |
| kh7002 | 44.3 | 205.2 | 98.0 | 164.0 | 9.4 | 18.4 | 58.6 | -49.2 | 0.020 |
| pol7001 | 43.9 | 205.4 | 49.0 | 164.0 | 58.6 | 18.4 | 58.3 | 0.3 | 0.020 |
| *South of Surveyor F.Z. and North of Mendocino F.Z.* | | | | | | | | | |
| cmapsu5b.a | 41.1 | 202.6 | 85.0 | 163.0 | 24.3 | 18.4 | 56.4 | -32.1 | 0.022 |
| cmapsu5b.b | 40.6 | 202.8 | 96.0 | 163.0 | 13.5 | 24.9 | 56.0 | -42.5 | 0.012 |
| *South of Pau F.Z. and North of Pioneer F.Z.* | | | | | | | | | |
| pol7201 | 38.9 | 216.1 | 49.0 | 168.0 | 57.9 | 13.2 | 57.3 | 0.6 | 0.035 |
| *South of Pioneer F.Z. and North of Murray F.Z.* | | | | | | | | | |
| pol7103.a | 35.7 | 218.4 | 46.0 | 169.0 | 61.2 | 13.2 | 55.8 | 5.4 | 0.035 |
| v2004 | 35.4 | 218.6 | 49.0 | 170.0 | 57.8 | 18.4 | 56.5 | 1.3 | 0.018 |
| indp16wt | 35.2 | 218.6 | 60.0 | 170.0 | 46.8 | 39.6 | 56.3 | -9.5 | 0.004 |
| lusi01ar | 35.0 | 218.4 | 31.0 | 170.0 | 76.0 | 39.6 | 56.2 | 19.8 | 0.004 |
| indp01wt | 35.0 | 218.5 | 58.0 | 170.0 | 48.9 | 39.6 | 56.2 | -7.3 | 0.004 |
| nova01ar | 34.5 | 218.5 | 15.0 | 170.0 | 92.1 | 39.6 | 55.9 | 36.2 | 0.004 |
| pol7103.b | 33.1 | 218.7 | 40.0 | 170.0 | 67.5 | 13.2 | 54.8 | 12.7 | 0.037 |
| gecs-amv | 32.9 | 218.8 | 86.0 | 170.0 | 21.5 | 18.4 | 54.6 | -33.1 | 0.019 |
| *South of Murray F.Z. and North of Molokai F.Z.* | | | | | | | | | |
| elt30 | 29.7 | 211.9 | 63.0 | 167.0 | 48.2 | 24.9 | 49.0 | -0.8 | 0.013 |
| cato01mv | 28.8 | 212.1 | 30.0 | 167.0 | 81.6 | 18.4 | 47.9 | 33.7 | 0.025 |
| si933010 | 27.4 | 212.4 | 22.0 | 168.0 | 89.5 | 39.6 | 47.2 | 42.4 | 0.006 |
| c1301.a | 27.0 | 212.3 | 60.0 | 168.0 | 51.7 | 39.6 | 46.7 | 5.0 | 0.006 |
| ztes07ar | 26.5 | 212.4 | 34.0 | 168.0 | 77.9 | 39.6 | 46.0 | 32.0 | 0.006 |
| c1301.b | 26.1 | 212.4 | 73.0 | 168.0 | 39.1 | 13.2 | 45.3 | -6.2 | 0.058 |
| dsdp18gc | 25.9 | 212.5 | 89.0 | 168.0 | 23.2 | 18.4 | 45.0 | -21.7 | 0.030 |
| erdc01wt | 25.8 | 212.5 | 89.0 | 168.0 | 23.3 | 18.4 | 44.7 | -21.4 | 0.031 |

**Table 1.** (*Continued.*)

| Profile | Lat (°N) | Long (°E) | Δθ(°) | Azim (°) | Datum $e_a$(°) | $\sigma_\theta$(°) | Model $e_m$(°) | Residual(°) | Importance |
|---|---|---|---|---|---|---|---|---|---|
| um6503-a | 25.5 | 212.8 | 54.0 | 168.0 | 58.4 | 18.4 | 44.3 | 14.2 | 0.031 |
| dsdp55gc.a | 24.8 | 213.0 | 46.0 | 168.0 | 66.8 | 18.4 | 43.0 | 23.8 | 0.033 |
| scan05ar | 24.4 | 213.0 | 59.0 | 168.0 | 54.1 | 13.2 | 42.2 | 11.9 | 0.067 |
| nova10ar | 24.3 | 212.9 | 60.0 | 168.0 | 53.1 | 18.4 | 42.1 | 11.0 | 0.035 |
| Subtotal | | | | | | | | | 0.772 |
| *Seafloor Created by Pacific - Farallon Spreading (Central)* | | | | | | | | | |
| *South of Molokai F.Z. and North of Clarion F.Z.* | | | | | | | | | |
| 74010908 | 20.6 | 221.2 | 90.0 | 171.0 | 22.0 | 39.6 | 38.3 | -16.3 | 0.011 |
| yaq7402 | 20.3 | 221.2 | 39.0 | 171.0 | 73.1 | 39.6 | 37.6 | 35.5 | 0.011 |
| epll01wt.a | 20.1 | 221.4 | 103.0 | 171.0 | 9.0 | 18.4 | 37.1 | -28.1 | 0.054 |
| 78123008 | 20.0 | 221.4 | 99.0 | 171.0 | 13.1 | 18.4 | 36.8 | -23.7 | 0.055 |
| kk047 | 20.0 | 221.4 | 99.0 | 171.0 | 13.1 | 18.4 | 36.8 | -23.7 | 0.055 |
| dpsn01wt.a | 19.6 | 221.5 | 63.0 | 171.0 | 49.6 | 18.4 | 35.8 | 13.8 | 0.060 |
| epll01wt.b | 19.5 | 221.4 | 53.0 | 171.0 | 59.5 | 24.9 | 35.3 | 24.1 | 0.034 |
| mons01ar | 17.7 | 221.8 | 87.0 | 171.0 | 27.1 | 24.9 | 29.9 | -2.7 | 0.052 |
| um6503-b | 16.8 | 222.1 | 73.0 | 171.0 | 42.0 | 18.4 | 26.6 | 15.3 | 0.118 |
| *South of Clarion F.Z. and North of Clipperton F.Z.* | | | | | | | | | |
| antp17mv | 8.4 | 216.9 | 221.0 | 169.0 | -89.5 | 39.6 | -27.0 | -62.5 | 0.103 |
| dsdp08gc | 6.2 | 217.6 | 152.0 | 169.0 | -14.4 | 39.6 | -39.7 | 25.2 | 0.091 |
| c1203 | 6.1 | 217.7 | 136.0 | 169.0 | 1.8 | 39.6 | -40.2 | 42.0 | 0.090 |
| *South of Clipperton F.Z. and North of Galapagos F.Z.* | | | | | | | | | |
| erdc11wt | 2.4 | 213.8 | 213.0 | 167.0 | -56.6 | 24.9 | -57.1 | 0.5 | 0.114 |
| aria01wt | 1.9 | 213.9 | 215.0 | 167.0 | -56.6 | 24.9 | -58.8 | 2.1 | 0.106 |
| Subtotal | | | | | | | | | 0.954 |
| *Seafloor Created by Pacific - Farallon Spreading (Southern)* | | | | | | | | | |
| *South of Galapagos F.Z. and North of Marquesas F.Z.* | | | | | | | | | |
| crgn02wt.c † | -6.4 | 218.0 | 281.0 | 168.0 | -80.5 | 39.6 | -77.4 | -3.1 | 0.017 |
| crgn02wt.b † | -8.1 | 218.2 | 332.0 | 168.0 | -124.4 | 39.6 | -79.6 | -44.8 | 0.014 |
| dsdp09gc | -8.5 | 218.2 | 349.0 | 168.0 | -139.1 | 39.6 | -80.1 | -59.0 | 0.014 |
| scan09ar | -9.1 | 218.2 | 266.0 | 168.0 | -53.8 | 18.4 | -80.8 | 27.1 | 0.061 |
| 72001831 | -9.9 | 218.5 | 329.0 | 168.0 | -113.7 | 18.4 | -81.7 | -32.0 | 0.057 |
| dolp02ho | -10.2 | 218.6 | 278.0 | 168.0 | -61.9 | 39.6 | -82.0 | 20.2 | 0.012 |
| crgn02wt.a † | -11.9 | 218.9 | 282.0 | 168.0 | -61.1 | 39.6 | -83.7 | 22.6 | 0.011 |
| *South of Marquesas F.Z. and North of Austral F.Z.* | | | | | | | | | |
| gecs-jmv | -17.7 | 214.1 | 314.0 | 165.0 | -82.2 | 18.4 | -87.1 | 4.8 | 0.034 |
| c1111 | -17.9 | 214.1 | 341.0 | 165.0 | -108.6 | 18.4 | -87.2 | -21.4 | 0.034 |
| c1306 | -18.0 | 214.3 | 324.0 | 165.0 | -91.7 | 18.4 | -87.3 | -4.4 | 0.033 |
| sotw01wt | -18.9 | 214.5 | 333.0 | 165.0 | -99.4 | 13.2 | -87.8 | -11.6 | 0.063 |
| c1714 | -19.5 | 214.8 | 337.0 | 165.0 | -102.8 | 18.4 | -88.1 | -14.8 | 0.032 |
| 72110807 | -20.2 | 215.1 | 320.0 | 165.0 | -84.8 | 18.4 | -88.5 | 3.7 | 0.031 |
| cato04mv | -20.6 | 215.2 | 316.0 | 165.0 | -80.2 | 24.9 | -88.7 | 8.4 | 0.017 |
| c1502 | -21.1 | 214.9 | 275.0 | 165.0 | -38.5 | 39.6 | -89.1 | 50.5 | 0.007 |
| scan08ar | -21.4 | 214.9 | 284.0 | 165.0 | -47.2 | 39.6 | -89.2 | 42.0 | 0.006 |
| *South of Austral F.Z. and North of Resolution F.Z.* | | | | | | | | | |
| v2104 | -28.0 | 214.9 | 292.0 | 163.0 | -50.2 | 39.6 | -91.3 | 41.1 | 0.005 |
| elt29 | -28.2 | 215.0 | 332.0 | 163.0 | -89.9 | 39.6 | -91.4 | 1.5 | 0.005 |
| *South of Resolution F.Z. and North of Agassiz F.Z.* | | | | | | | | | |
| pol6702 | -35.1 | 217.7 | 1.0 | 161.0 | -116.1 | 24.9 | -92.8 | -23.2 | 0.013 |
| Subtotal | | | | | | | | | 0.466 |
| *Seafloor Created by Pacific - Bellingshausen Spreading* | | | | | | | | | |
| *West of V F.Z. and East of Heezen F.Z.* | | | | | | | | | |
| c1212 | -48.5 | 218.5 | 14.0 | 216.0 | -99.1 | 13.2 | -113.4 | 14.3 | 0.050 |
| v3601.a | -49.4 | 217.3 | 2.0 | 216.0 | -87.9 | 18.4 | -113.1 | 25.2 | 0.026 |
| *West of Heezen F.Z. and East of Tharp F.Z.* | | | | | | | | | |
| v3601.b | -48.7 | 211.9 | 33.0 | 216.0 | -118.7 | 18.4 | -113.6 | -5.1 | 0.025 |
| *West of Tharp F.Z. and East of Udintsev F.Z.* | | | | | | | | | |
| elt33 | -50.0 | 203.0 | 75.0 | 217.0 | -161.0 | 39.6 | -113.9 | -47.1 | 0.005 |
| end.a408n ‡ | -50.0 | 202.7 | 29.0 | 217.0 | -115.0 | 39.6 | -113.9 | -1.1 | 0.005 |
| elt23 | -50.2 | 202.6 | 13.0 | 217.0 | -98.9 | 18.4 | -113.9 | 14.9 | 0.025 |
| *West of Udintsev F.Z.* | | | | | | | | | |
| elt19 | -50.9 | 195.4 | 25.0 | 217.0 | -111.5 | 18.4 | -114.1 | 2.6 | 0.024 |
| end.a408s ‡ | -51.4 | 195.1 | 359.0 | 218.0 | -85.6 | 39.6 | -114.2 | 28.6 | 0.005 |
| elt25 | -52.1 | 193.9 | 30.0 | 218.0 | -116.8 | 18.4 | -114.1 | -2.7 | 0.024 |
| end.odf6 ‡ | -52.2 | 194.0 | 83.0 | 218.0 | -169.9 | 39.6 | -114.1 | -55.8 | 0.005 |
| end.v16 ‡ | -53.3 | 193.1 | 52.0 | 220.0 | -138.9 | 39.6 | -114.0 | -24.9 | 0.005 |
| um66-b | -53.4 | 191.5 | 41.0 | 219.0 | -128.1 | 18.4 | -113.9 | -14.2 | 0.024 |
| Subtotal | | | | | | | | | 0.223 |
| *Seafloor Created by Pacific - Antarctica Spreading* | | | | | | | | | |
| *East of Endeavor F.Z.* | | | | | | | | | |
| end.odf8 ‡ | -55.1 | 191.6 | 54.0 | 241.0 | -135.8 | 39.6 | -116.4 | -19.4 | 0.005 |
| elt43 | -56.0 | 187.3 | 1.0 | 244.0 | -83.1 | 13.2 | -116.4 | 33.3 | 0.048 |
| um6402-b | -56.2 | 187.1 | 14.0 | 244.0 | -96.0 | 24.9 | -116.4 | 20.3 | 0.014 |
| gecs-gmv | -56.6 | 184.9 | 37.0 | 246.0 | -119.3 | 18.4 | -116.4 | -2.9 | 0.025 |
| end.w ‡ | -56.5 | 184.7 | 22.0 | 246.0 | -104.2 | 39.6 | -116.5 | 12.3 | 0.005 |
| end.l | -57.3 | 180.5 | 97.0 | 250.0 | -179.3 | 39.6 | -116.5 | -62.8 | 0.005 |
| *West of Endeavor F.Z. and East of the continuation of XII F.Z.* | | | | | | | | | |
| end.f | -58.5 | 177.3 | 355.0 | 253.0 | -77.9 | 39.6 | -116.2 | 38.2 | 0.005 |
| end.k.a | -58.3 | 176.8 | 348.0 | 253.0 | -70.9 | 39.6 | -116.3 | 45.4 | 0.005 |

**Table 1.** (*Continued.*)

| Profile | Lat (°N) | Long (°E) | Δθ(°) | Azim (°) | Datum $e_a$(°) | $\sigma_\theta$(°) | Model $e_m$(°) | Residual(°) | Importance |
|---|---|---|---|---|---|---|---|---|---|
| *West of the continuation of XII F.Z. and East of the continuation of XIII F.Z.* | | | | | | | | | |
| end.k.b | -59.2 | 177.0 | 55.0 | 253.0 | -138.4 | 24.9 | -115.8 | -22.6 | 0.013 |
| end.s | -59.3 | 176.0 | 20.0 | 255.0 | -103.3 | 18.4 | -115.9 | 12.6 | 0.024 |
| dsdp28gc | -59.4 | 175.5 | 17.0 | 255.0 | -100.5 | 24.9 | -115.9 | 15.4 | 0.013 |
| end.q | -59.0 | 175.0 | 356.0 | 255.0 | -79.2 | 39.6 | -116.1 | 36.9 | 0.005 |
| end.d | -58.9 | 174.8 | 354.0 | 255.0 | -77.2 | 39.6 | -116.1 | 38.9 | 0.005 |
| elt52 | -59.1 | 174.1 | 53.0 | 256.0 | -136.3 | 13.2 | -116.1 | -20.2 | 0.048 |
| end.c.a | -59.4 | 173.0 | 51.0 | 257.0 | -134.4 | 18.4 | -116.0 | -18.4 | 0.024 |
| end.b | -59.5 | 172.8 | 40.0 | 257.0 | -123.5 | 18.4 | -115.9 | -7.6 | 0.024 |
| *West of the continuation of XIII F.Z.* | | | | | | | | | |
| end.c.b | -60.2 | 172.9 | 44.0 | 258.0 | -127.8 | 24.9 | -115.6 | -12.2 | 0.013 |
| end.v ‡ | -60.5 | 172.2 | 104.0 | 259.0 | -188.0 | 39.6 | -115.4 | -72.6 | 0.005 |
| end.p | -60.7 | 171.1 | 34.0 | 260.0 | -118.1 | 18.4 | -115.4 | -2.6 | 0.024 |
| elt32 | -60.7 | 171.0 | 0.0 | 260.0 | -84.0 | 24.9 | -115.4 | 31.4 | 0.013 |
| end.n | -60.8 | 170.0 | 40.0 | 261.0 | -124.1 | 24.9 | -115.4 | -8.7 | 0.013 |
| Subtotal | | | | | | | | | 0.336 |
| Total | | | | | | | | | 2.992 |

The error covariance matrix has units of degrees squared. The covariance matrix is described in a global Cartesian coordinate system with the origin at the centre of the Earth, the $x$ axis parallel to 0°N, 0°E, the $y$ axis parallel to 0°N, 90°E, and the $z$ axis parallel to 90°N. The apparent effective inclination, $e_a$, was obtained from the phase shift $\Delta\theta$ using eq. (1), where $\Delta\theta$ is the quantity opposite of Schouten & Cande's (1976) $\theta$.

* Letters in parentheses following CMAPSU4S profiles are names used by Grim & Erickson (1969; Figs 2, 3, 5, and 6). † Profiles digitized from Kruse (1988). ‡ Profiles digitized from Christoffel & Falconer (1972).

The skewness analysis of these profiles is mainly straightforward, but less so than the analysis of the eastern Pacific–Kula anomalies, which have higher amplitudes. The phase shifts we estimate range from 15° to 98° with most between 40° and 70° (Fig. 4). Eight profiles were rated category A, 14 category B, four category C, and seven category D.

### *Central Pacific–Farallon crossings*

The 19 profiles analysed in this group lie south of the Molokai fracture zone and north of the Galapagos fracture zone (Fig. 2d). The peak-to-trough amplitudes of these profiles range from 100 to 200 nT (Fig. 5). They are the lowest amplitude data that we used. The separation between anomaly 27 and 25 indicates spreading half-rates of 29–33 mm yr$^{-1}$, ~25 per cent slower than the 42 mm yr$^{-1}$ spreading half-rate predicted by the model of Engebretson *et al.* (1984) and close to the 32–33 mm yr$^{-1}$ rates predicted by Rosa & Molnar (1988) (Fig. 10).

The 11 northernmost profiles lie north of the Clarion fracture zone. Their identifications and locations are consistent with those shown by Atwater & Severinghaus (1989) north of the Clarion and south of a short unnamed fracture zone just south of the Molokai fracture zone. From this group, we rejected profile C2002 because of its very low amplitude, and profile DPSN01WT.b because of the double peak to the east of anomaly 25r that makes its skewness estimate questionable. Published maps show no identifications of early Tertiary anomalies south of the Clarion and north of the Clipperton fracture zone and only sparse tentative identifications of anomalies south of the Clipperton and north of the Galapagos fracture zone. This lack of identified anomalies can be attributed to three causes. First and most important, the amplitudes of the anomalies are very low. Second, magnetic profiles are sparse in this region relative to sea-floor farther north. Third, as Acton & Gordon (1991) have shown, the remanent effective inclination of the sea-floor in this region, and therefore the skewness of its magnetic anomalies, is expected to change rapidly from north to south, making it difficult to correlate the same anomaly over a long distance. All these reasons make anomaly identification, and the estimates of their skewness, risky in this region.

None the less, we tentatively identify, and estimate the skewnesses of, five crossings of anomaly 25r: three north of the Clipperton fracture zone and two south of the Clipperton fracture zone (Figs 5 and 11). Two of these profiles were previously used by Acton & Gordon (1991), who made tentative correlations and skewness estimates of part of the anomaly sequence from 27r to 31. We assign three of our skewness estimates to category D and two (ERDC11WT, which we consider to be the best of these crossings, and ARIA01WT) to category C. Our estimate of the phase shift of the two profiles south of the Clipperton differs by an average of 70° from those north of the Clipperton, whereas the two groups of profiles differ in latitude (and palaeolatitude) by only about 4°. Part of the difference (20–25°) is expected from the changes in the effective inclination of the Earth's present field and an approximately equal amount is expected from the change with palaeolatitude of the remanent effective inclination, leaving about a 20° difference to be explained by error. Two additional crossings north (KK049 and PLDS03MV) and one additional crossing (V2403) south of the Clipperton fracture zone were rejected because of their questionable correlations, low amplitudes, and skewnesses inconsistent with nearby crossings.

### *Southern Pacific–Farallon crossings*

The 21 profiles analysed in this group lie south of the Galapagos fracture zone and all but four lie north of the Austral fracture zone (Fig. 2e). These profiles have peak-to-trough amplitudes of about 200–400 nT (Fig. 6). The observed half-rates obtained from the separation of anomalies 25 and 27 range from 19 mm yr$^{-1}$ to 32 mm yr$^{-1}$. These rates can be further subdivided into a northern and southern subgroup with an abrupt transition between profiles CATO04MV and C1502 (~21°S; Fig. 10). The northern rates range from 26 to 32 mm yr$^{-1}$, while the southern rates range from 19 to 21 mm yr$^{-1}$. The spreading half-rates predicted by the model of Engebretson *et al.* (1984) range from ~24 mm yr$^{-1}$ (in the south) to ~38 mm yr$^{-1}$ (in the north), and those predicted by the model of Rosa & Molnar (1988) between ~22 mm yr$^{-1}$ (in the south) and ~31 mm yr$^{-1}$ (in the north) (Fig. 10). The observed rates mimic the pattern of decreasing half-spreading rates from north to south, but are consistently slower than the predictions of both models. A group of seven rates from profiles near 20°S are distinctly faster than this trend, however. This observation weakens the conclusion of Engebretson *et al.* (1984) and Rosa & Molnar (1988) that the Pacific and Farallon plates both were single rigid plates during this interval. Alternatively, the data are consistent with two rigid plates if spreading near 20°S was

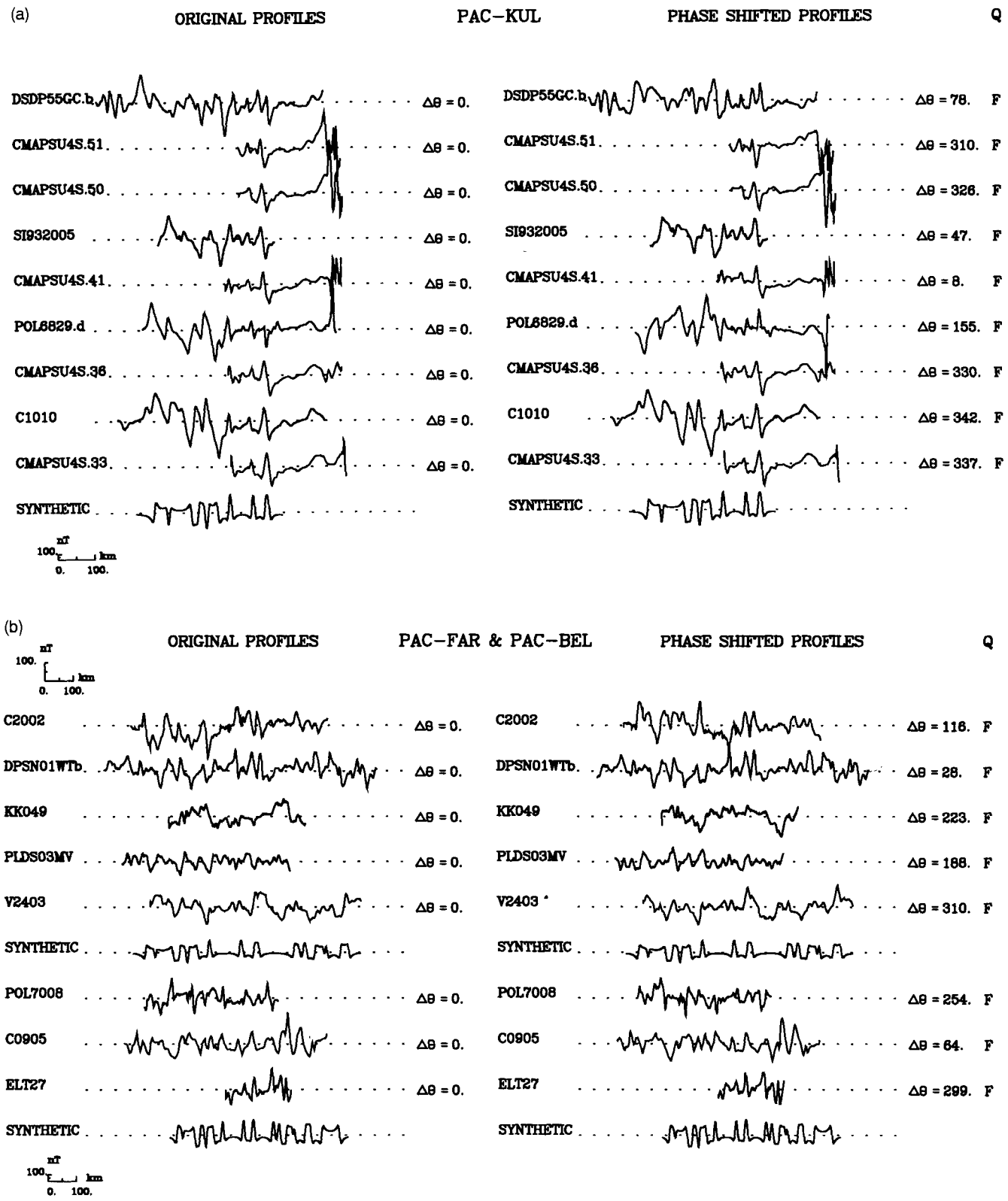


**Figure 9.** Profiles not used to estimate the chron 25r palaeomagnetic pole. (a) Profiles DSDP55GC.b through CMAPSU4S.33 were recorded over Pacific–Kula sea-floor. The synthetic profiles show the sequence from (normal) anomaly 31 (on the left) to (normal) anomaly 25 (on the right). (b) Profiles C2002–V2403 were recorded over central Pacific–Farallon sea-floor, profiles POL7008–C0905 over southern Pacific–Farallon sea-floor, and profile ELT27 over Pacific–Bellingshausen sea-floor. The scale bars on the top of the figure correspond to profiles C2002 through V2403, whereas the scale bars on the bottom of the page correspond to profiles POL7008 through ELT27. The synthetic profiles show the sequence from (normal) anomaly 31 (on the left) to (normal) anomaly 22 (on the right) in the middle of the figure and to (normal) anomaly 21 at the bottom of the figure.

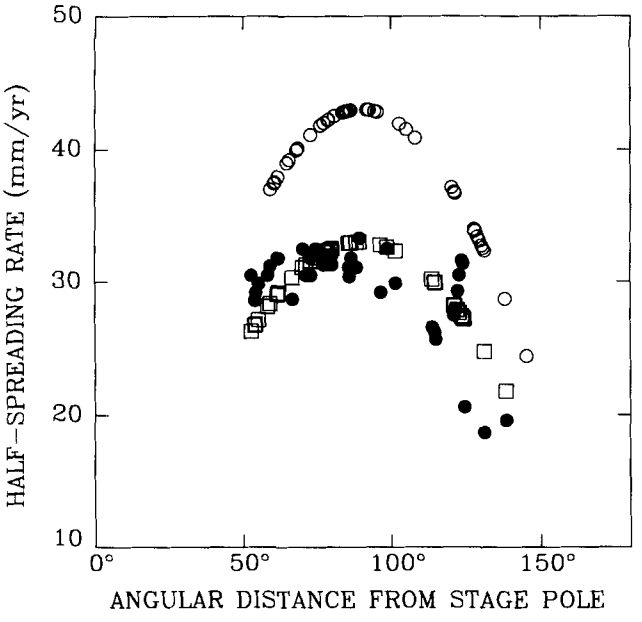


**Figure 10.** Observed (●) and predicted (○: Engebretson *et al.* 1984; □: Rosa & Molnar 1988) half-spreading rates versus distance from the stage pole of rotation for Pacific–Farallon crossings. The observed rates were estimated from the distance between anomaly 27 and 25 on each of the profiles that we analysed. The seven inconsistently fast rates near an angular distance of 120° from the stage pole of rotation are associated with an increase southwards in spreading rates between the Marquesas and Austral fracture zones followed by an abrupt decrease in spreading rate just north of the Austral fracture zone.

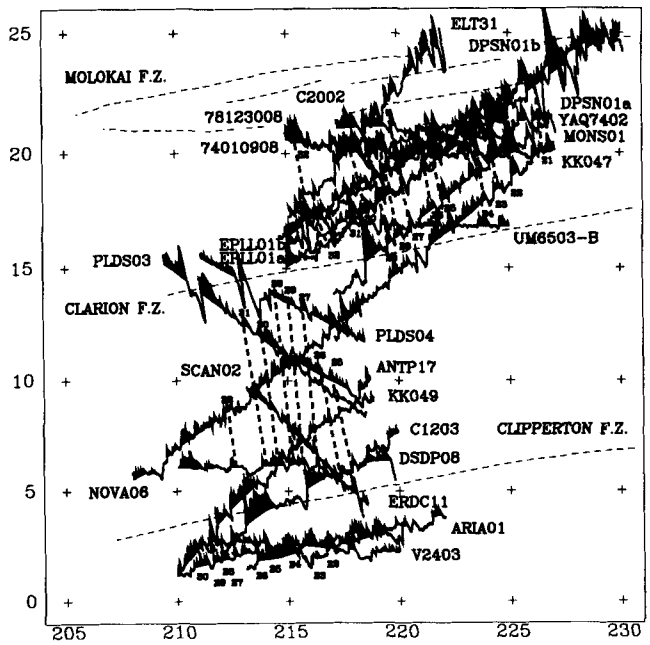


**Figure 11.** Map of newly correlated magnetic profiles obtained over the central Pacific–Farallon region. The profiles were phase shifted by the amount predicted by the model for anomaly 25r. These model phase shifts were 70–91° between the Molokai and Clarion fracture zones, 130–183° between the Clarion and Clipperton fracture zones, and 216–220° between the Clipperton and Galapagos fracture zones. Positive anomalies are shaded solid black and negative anomalies are unshaded. The anomalies have been projected onto a lineation-parallel direction. The thick dashed lines indicate our anomaly correlations. (Mercator projection.)

highly asymmetric. The documentation of ridge jumps and asymmetrical spreading for younger pacific–Nazca anomalies 18–21 south of this region (Cande & Haxyb 1991) may make the latter scenario the more likely of the two.

Some profiles show extra complications. There is a pronounced positive anomaly between anomalies 26 and 27 on profiles DOLP02H0 and DSDP09GC, and smaller peaks of similar shape between anomalies 26 and 27 on profiles 72001831 and SCAN09AR. Our identifications of anomalies 25 and 26 for these profiles are consistent with those of Kruse (1988), but because of the lower quality of profiles DOLP02HO and DSDP09GC they were assigned to category D. There is a pronounced extra peak east of anomaly 25 on profiles GECS-JMV and C1111, that can also be traced to a smaller peak on profile C1306. The bathymetry of all three profiles shows a seamount or ridge over 2 km in height underlying these anomalies. As these profiles are all immediately west of the Tuamotu plateau, the extra anomalies likely mark the western edge of the plateau. We rejected profile POL7008 because of the atypical appearance of anomaly 25r, and profile C0905 because of its inconsistency with nearby crossings. We did not deskew profile C0806 (shown by an open circle at 42°S on Fig. 2a) because of a large data gap that spans most of anomalies 25r and 26.

These profiles are higher in quality for skewness analysis than the central Farallon anomalies mainly because of their higher amplitudes, but they are not as good as the northern Farallon profiles because of slower spreading rates and greater sea-floor roughness, especially between the Marquesas and Austral fracture zones. One profile was rated category A, seven category B, two category C, and nine category D. Three of the category D profiles were digitized from published figures (Kruse 1988). The phase shifts range from 266° to 1° (i.e. within the 95° wide interval between −94° and +1°) (Fig. 6).

### Pacific–Bellingshausen crossings

The 12 profiles analysed in this group lie west of fracture zone V and east of the magnetic bight separating sea-floor created by Pacific–Antarctic and Pacific–Bellingshausen spreading (at 191–192°E, between the Endeavor and Udintsev fracture zones) (Fig. 2f). These profiles have peak-to-trough amplitudes of about 200–400 nT (Fig. 7). The observed half-rates obtained from the separation of anomalies 25–27 range from 26 to 31 mm $yr^{-1}$. The anomaly 31–25 stage pole and angular rate calculated from the finite rotations of Stock & Molnar (1982) predict half-rates of 25 mm $yr^{-1}$ (in the west) to 37 mm $yr^{-1}$ (in the east), while the anomaly 28–25 stage pole and angular rate calculated from the finite rotations of Mayes, Lawver & Sandwell (1990) predict half-rates of 24–33 mm $yr^{-1}$.

These profiles are similar in skewness-analysis quality to the southern Farallon ones, mainly because of their similar amplitudes. One profile was assigned to category A, six to category B, and five to category D. Four of the category D profiles were digitized from published figures (Christoffel &

Falconer 1972). Their phase shifts range from −1° to 83° with most between 10° and 40° (Fig. 7).

### Pacific–Antarctic crossings

The 22 profiles analysed in this group lie west of the magnetic bight separating Pacific–Antarctic from Pacific–Bellingshausen sea-floor (191–192°E) and east of 169° (Fig. 2g). These profiles have peak-to-trough amplitudes of about 200-400 nT (Fig. 8). The observed half-rates obtained from the separation of anomalies 25–27 range from 17–21 mm $yr^{-1}$ west of the Endeavor fracture zone to 25–28 mm $yr^{-1}$ east of the Endeavor fracture zone. The anomaly 31–25 stage pole and angle of Stock & Molnar (1987) predict half-rates of 22 mm $yr^{-1}$ (in the west) to 28 mm $yr^{-1}$ (in the east), while the anomaly 28–25 stage pole and angular rate calculated from the finite rotations of Mayes *et al.* (1990) predict half-rates of 13–17 mm $yr^{-1}$.

These profiles are similar in skewness-analysis quality to the Bellingshausen ones. Two profiles were rated category A, five category B, six category C, and eight category D. Three of the category D profiles were digitized from published figures (Christoffel & Falconer 1972). The phase shifts range from −12° to 104° with most between 20° and 50° (Fig. 8). Profile ELT27 was rejected because of the inconsistency of its skewness estimate with nearby crossings.

This region of Pacific sea-floor is characterized by many short offsets such as the one between profiles END.Q and DSDP28GC (Fig. 2g). These short offsets are associated with rough sea-floor topography and may help explain some of the scatter in the estimated phase shifts. The roughness is also a potential source of error in estimated transform azimuths used to calculate effective remanent inclinations from phase shifts.

## RESULTS

### Main palaeomagnetic results

If equal weight is given to each of the 132 acceptable skewness estimates, the best-fit pole is located at 78.9°N, 9.4°E with a 95 per cent confidence ellipse that has a 6.7° major semi-axis striking N76°E and a 4.7° minor semi-axis. The best-fit value of anomalous skewness is 14.5° ± 5.8° (95 per cent confidence level). The estimated standard deviation of the data is 27.9°.

When the 132 acceptable data are divided into their four quality categories, the estimated standard deviations are 13.2° for the 16 data in category A, 18.4° for the 44 data in category B, 24.9° for the 29 data in category C, and 39.6° for the 43 data in category D. The best-fitting poles from only the data in each category are 74.3°N, 33.6°E for category A, 77.7°N, 351.0°E for category B, 79.7°N, 7.6°E for category C, and 79.7°N, 33.5°E for category D. These poles differ insignificantly from one another (Fig. 12). Assigning these standard deviations to each input datum and inverting the 132 acceptable data gives the preferred best-fit pole at 78.2°N, 4.8°E with a 95 per cent confidence ellipse that has a 6.4° major semi-axis striking N93°E and a 4.1° minor semi-axis (Fig. 12). This second pole lies only 1.2° arc-length from the pole estimated when each datum was given equal weight. The best-fit value of anomalous skewness is

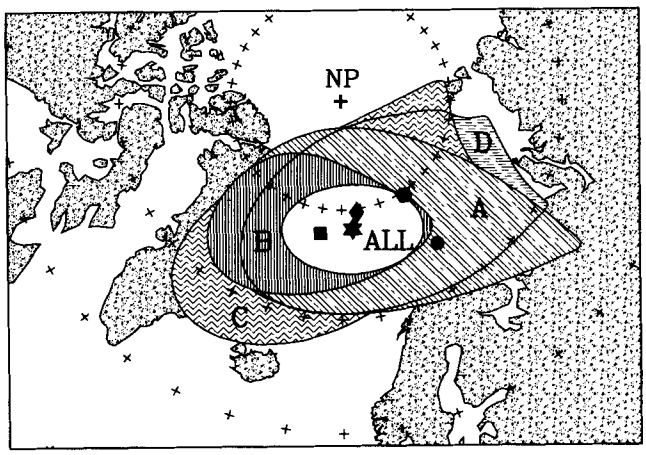


**Figure 12.** Palaeomagnetic poles and associated confidence limits for data subsets A (●, diagonal stripes), B (■, vertical stripes), C (◆, zig-zag lines) and D (●, dashed lines). These four subsets correspond to four quality rankings with A being the best and D the worst. The best-fitting pole from all data (★) and its associated 95 per cent confidence limits (unshaded) are also shown. The confidence limits of subsets A–D were computed using the technique of constant-chi-square boundaries.

16.2° ± 4.6° (95 per cent confidence level). The statistic $\chi^2$ has a value of 128.6 with 129 degrees of freedom. Table 1 gives these parameters, as well as the observed and model apparent effective inclinations, data residuals, and data importances for each anomaly crossing. The normalized residuals for each quality group are shown in Fig. 13.

If all 149 phase shifts, including those that we rejected, are inverted, the best-fit pole is located at 77.9°N, 9.1°E with a 95 per cent confidence ellipse that has a 6.2° major semi-axis striking N95°E and a 3.8° minor semi-axis. The best-fit value of anomalous skewness is 16.5° ± 4.6° (95 per cent confidence level). For this calculation, the 17 phase shifts that were previously rejected (quality group F) were assigned standard deviations of 74.1°, which is the estimated standard deviation found by inverting them alone. If only the quality group A and B data are used, the best-fit pole is located at 77.5°N, 8.3°E with a 95 per cent confidence ellipse that has a 9.5° major semi-axis striking N102°E and a 4.4° minor semi-axis. The best-fit value of anomalous skewness is 17.5 ± 5.3° (95 per cent confidence level). Both of these poles are located no more than 1.0° arc-length from the preferred pole and differ insignificantly from it.

Allowing anomalous skewness to adjust instead of fixing it at zero decreases $\chi^2$ from 177.4 to 128.6, which is a 27.5 per cent reduction of variance and gives a value of $F$ of 48.9 with 1 versus 129 degrees of freedom in the test for the significance of anomalous skewness as an additional adjustable parameter. The probability of $F$ being this large or larger by chance is $1.3 \times 10^{-01}$; thus the improvement in fit is highly significant. Although this proves neither that anomalous skewness is uniform nor that it is independent of spreading rate and other variables, it shows that this simple one-parameter adjustment can explain a considerable amount of the variance in the data. The 16.2° ± 4.6° (95 per cent confidence limits) value we obtain for anomalous skewness agrees well with prior estimates. With our

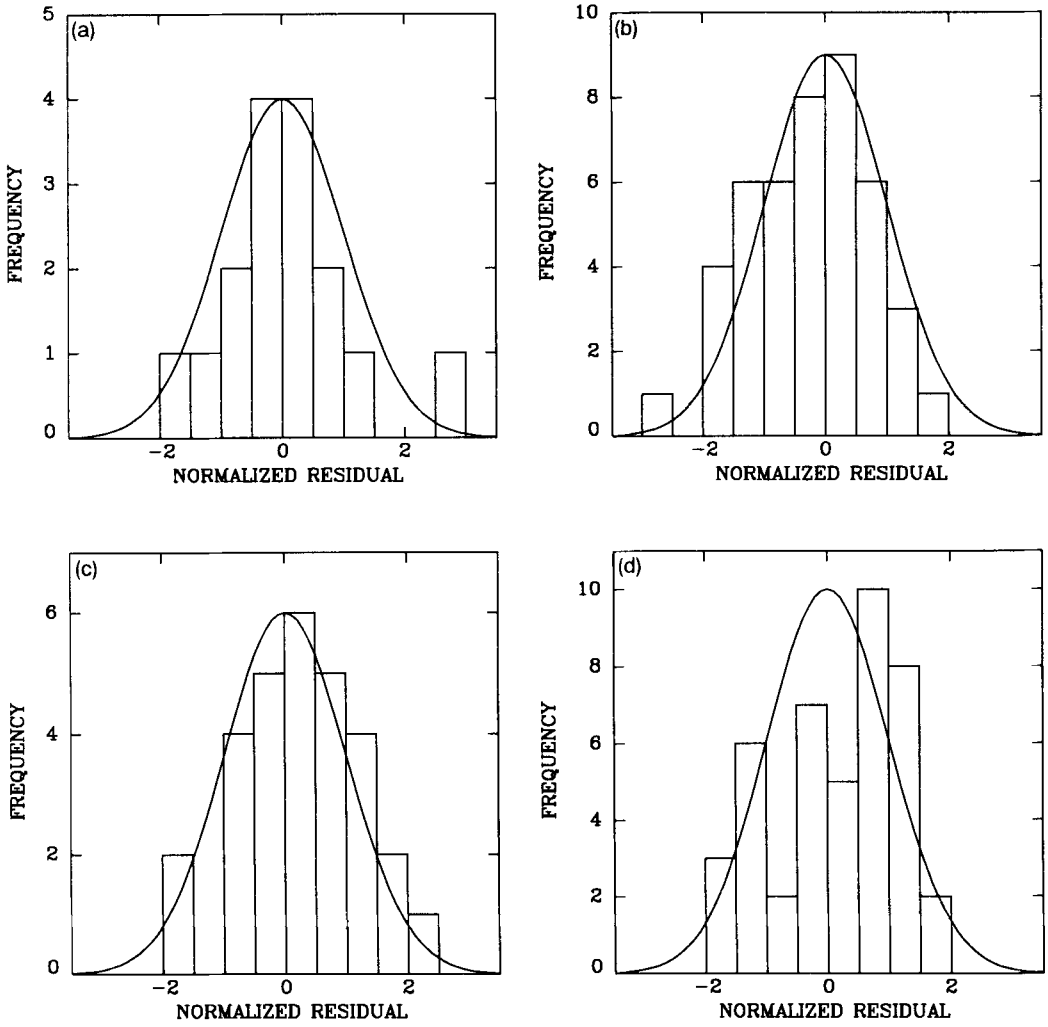


**Figure 13.** Histograms of normalized residuals of the data (i.e. residuals divided by the population standard deviations) within each quality category. The population standard deviations are 13.2° for group A, 18.4° for group B, 24.9° for group C, and 39.6° for group D.

assumption that it has an equal value for all anomaly 25r crossings we would predict an across-ridge discrepancy of 32.4° ± 9.2°, consistent with the across-ridge discrepancy of 12–28° found by Cande (1976) for the sequence of anomalies 27 to 32.

Regional constraints on the pole position and the systematic nature of anomalous skewness are illustrated in Figs 14(a) and (b). To make these figures, the data were divided into the same six tectonic and geographic regions as in the discussion above, i.e. (1) Pacific–Kula profiles, (2) northern Pacific–Farallon profiles (north of the Molokai fracture zone, ~22°N), (3) central Pacific–Farallon profiles (south of the Molokai but north of the Galapagos fracture zone, between the equator and ~22°N), (4) southern Pacific–Farallon profiles (south of the Galapagos fracture zone), (5) Pacific–Bellingshausen profiles, and (6) Pacific–Antarctic profiles. Fig. 14(a) shows how the data from the different regions constrain the pole position when no adjustment is made for anomalous skewness. If there were no errors in an observed skewness and if the true remanent effective inclination equalled the apparent remanent effective inclination, the phase shift of a single anomaly crossing would constrain the pole to lie on a great semicircle. The six great semicircles shown in Fig. 14(a) are averages for each of the six tectonic–geographic regions. If the data were free of errors, and if there were no anomalous skewness, the six great semicricles would intersect in a point, which they obviously do not. Fig. 14(b) shows the same six great semicircles after correction for the best estimate of assumed-uniform anomalous skewness. Although they still do not intersect at a point, their dispersion about the best-fitting point is greatly reduced and each regional average is fit within its 95 per cent confidence limits.

Because there are many input data, the pole has small confidence limits and is formally comparable in accuracy to poles averaged from several seamount poles and to the highest-quality poles obtained on land by traditional palaeomagnetic methods. Unlike seamount poles and typical palaeomagnetic studies on land, the age of the pole is precisely known. Moreover, the geographical distribution of sites is much broader than for any palaeomagnetic pole on land or from seamounts, making it likely that many types of systematic errors are smaller in this new pole than in poles from other types of palaeomagnetic data, and are already

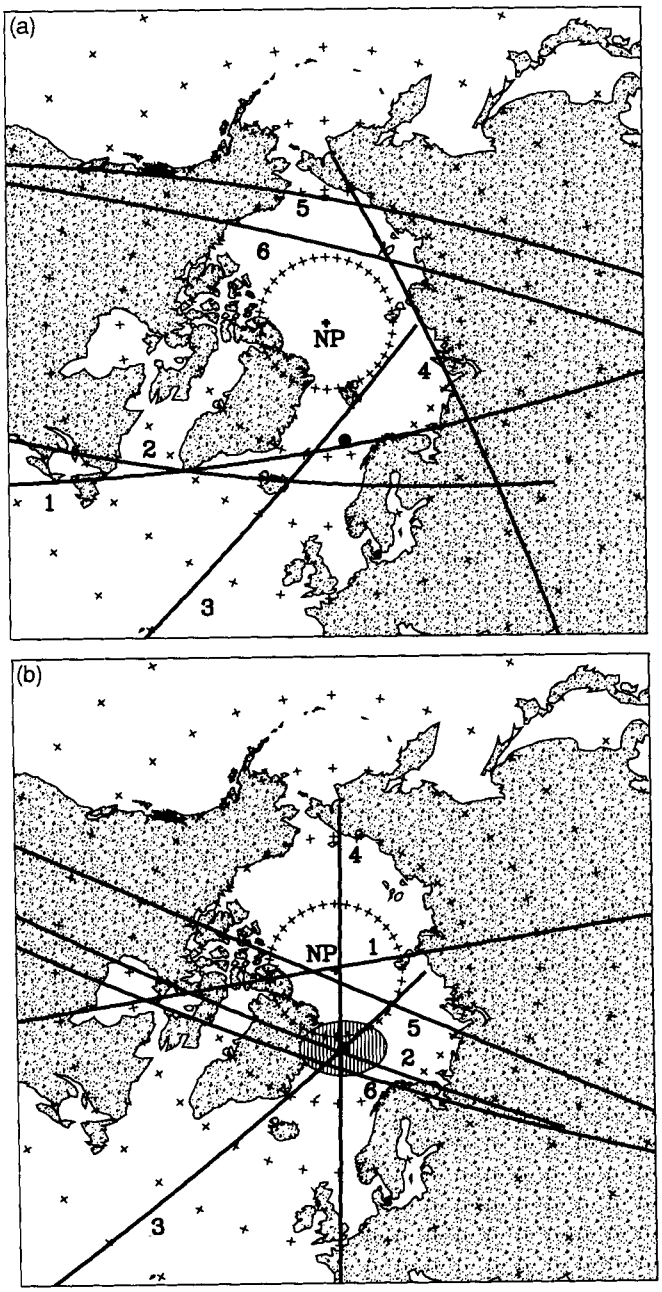


**Figure 14.** (a) Map of the northern polar region showing loci of pole positions consistent with the mean effective inclination from each of the six tectonic-geographic regions. Each locus is a great semicircle of possible pole positions, whose tip is located 90° away from the anomaly's location along the great circle tangent to the lineation. These were obtained by taking the model predicted effective inclination for a representative location and adding to it the average regional residual. Profile 1 (CMAPSU4S.13) is representative of Pacific–Kula spreading; profiles 2 (POL7201), 3 (ANTP17MV) and 4 (CATO04MV) of northern, central and southern Pacific–Farallon spreading respectively; profile 5 (ELT33) of Pacific–Bellingshausen spreading; and profile 6 (END.L) of Pacific–Antarctica spreading. For anomalous skewness equal to zero the best-fitting pole is located at 72.3°N, 8.5°E. (b) For anomalous skewness equal to its best-fitting value (16.2°) the agreement of the great semicircles improves with the three Pacific–Farallon great semicircles and the Pacific–Antarctic great semicircle nearly intersecting at a point near the best-fitting pole, which is located at 78.2°N, 4.8°E. (Stereographic projections, tick marks every 10°).

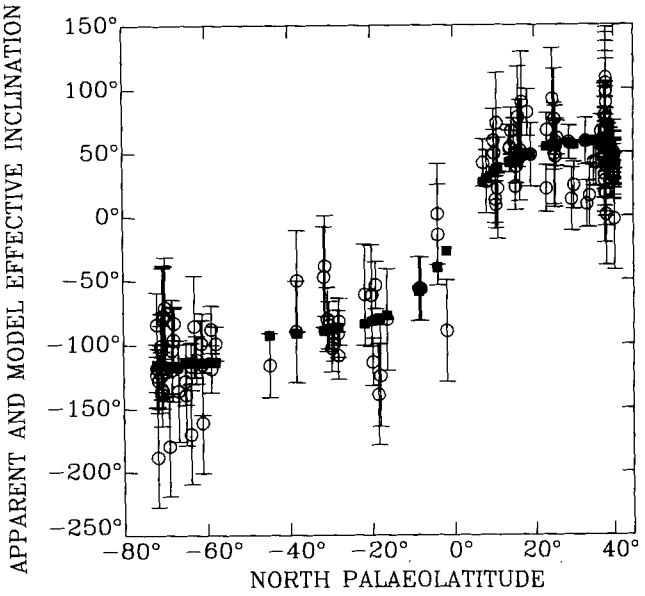


**Figure 15.** Comparison of the model (■) with the observed apparent (○) effective remanent inclinations for each useful anomaly 25r skewness estimate plotted against palaeolatitude. Corresponding remanent effective inclinations can be found by adding anomalous skewness (16.2° ± 4.6°) to these model effective remanent inclinations. The high gradient in observed (and in modelled) effective remanent inclination in low palaeolatitudes provides a strong constraint on the location of the palaeomagnetic pole position.

mainly reflected in its confidence limits, which is unlikely to be true for poles from seamount poles or from land-based palaeomagnetic studies.

Each observed apparent effective inclination (eq. 1) is compared with its corresponding model effective inclination (eq. 9) in Fig. 15, where both are plotted against site palaeolatitude calculated from the best-fitting palaeomagnetic pole. Recall that anomalous skewness must be added to the model effective inclination to infer the remanent magnetization. Model effective inclinations range from −116° for the easternmost Pacific–Antarctic crossings to +61° for the northernmost Pacific–Farallon crossings we analysed. In between, the model effective inclinations range from −116° to −115° for Pacific–Antarctic crossings, from −113° to −114° for Pacific–Bellingshausen crossings, from −93° to −77° for southern Pacific–Farallon crossings, from −59° to +38° for central pacific–Farallon crossings, from 42° to 61° for northern Pacific–Farallon crossings, and from 41° to 43° for Pacific–Kula crossings. Only the Pacific–Antarctic and Pacific–Bellingshausen crossings lie in high palaeolatitudes from 58°S to 72°S. The southern Pacific–Farallon crossings have palaeolatitudes from 45°S to 16°S, the central Farallon from 8°S to 11°N, and the northern Farallon from 14°N to 39°N. The Pacific–Kula crossings have nearly uniform palaeolatitudes of 38° to 40°N. Some of the data display considerable scatter, as suggested by the large errors we assigned to some of the data, but the misfit is mainly symmetrically dispersed about the values calculated for the best-fitting model, except for the Pacific–Kula crossings, for which the apparent effective inclinations tend to be 9° greater than the model effective inclinations, and for the Pacific–Bellingshausen crossings, for which the

apparent effective inclinations tend to be 5° less than the model effective inclinations (*cf.* Fig. 14b). Neither difference is statistically significant.

Linear propagation of errors will give inaccurate confidence limits if the linear approximation is poor, which is most likely to occur for sparse data sets and when the best-fitting pole lies near the tip of a great semicircle, which corresponds to a singularity in effective inclination and in chi-square (Petronotis *et al.* 1992). The apparent effective inclinations estimated for anomaly 25r are many and the anomaly crossings are well distributed; we thus expect to obtain an accurate confidence ellipse from linear propagation of errors. The 95 per cent confidence region calculated from constant-chi-square boundaries agrees well with the 95 per cent confidence ellipse calculated from linear propagation of errors (Fig. 16a). We furthermore checked the confidence limits found by linear propagation of errors with Monte Carlo simulations of the apparent effective inclination data (Fig. 16b). Of the 10 000 simulated best-fitting poles, 9461 fell within the 95 per cent confidence limits found by linear propagation of errors, supporting the usefulness of linear propagation of errors when applied to these data.

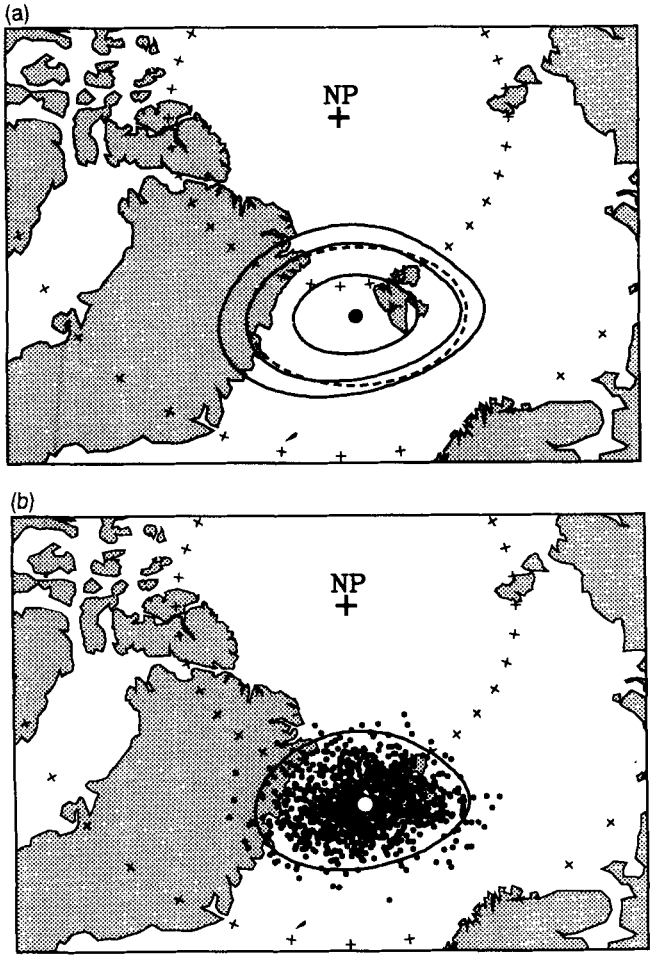


**Figure 16.** (a) Map of the northern polar region showing the chron 25r pole with its confidence regions. The dashed line is the 95 per cent confidence ellipse obtained from linear propagation of errors. The solid lines are the regions corresponding to the standard error (closest to the pole), 95 and 99 per cent (farthest from the pole) confidence levels, respectively, and were calculated using constant contours of $\chi^2$ (Petronotis *et al.* 1992). The 95 per cent confidence regions calculated using the two different methods are in excellent agreement. (b) Monte Carlo simulations of chron 25r pole: 9461 out of 10 000 simulated poles were included within the 95 per cent confidence limits of the pole. Here, we show a representative subset of 1000 simulations. (Polar stereographic projections, tick marks are every 10°.)

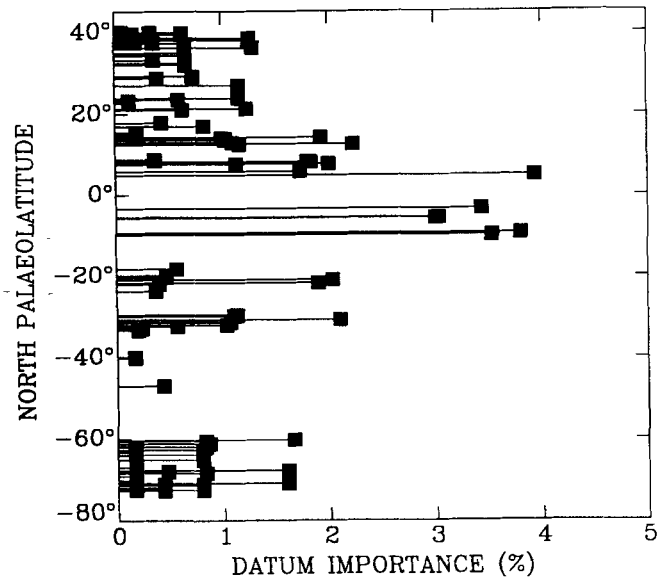


**Figure 17.** Datum importance versus palaeolatitude of each crossing of anomaly 25r used in estimating the chron 25r palaeomagnetic pole. The highest values between 5°N and 10°S show the high information content of the lowest palaeolatitude crossings, despite the large uncertainties assigned to their skewness estimates.

The central Pacific–Farallon data, with 32 per cent of the total importance, contribute more information than do any one of the other regions (Fig. 17, Table 1) presumably because in low palaeolatitudes, small changes in estimated pole position cause large changes in predicted values of effective inclination, an effect that outweighs the larger uncertainties that we assign to these data (also see Acton & Gordon 1991). The northern Pacific–Farallon data contribute 26 per cent of the information, the southern Pacific–Farallon data 16 per cent, the Pacific–Antarctic data 11 per cent, the Pacific–Kula data 8 per cent and the Pacific–Bellingshausen data 7 per cent. Because of the different numbers of data in each region, however, an average Pacific–Bellingshausen datum contributes more to the pole and anomalous skewness than does an average Pacific–Antarctic or Pacific–Kula datum. Central Pacific–Farallon profiles UM6503-B and ERDC11WT have the highest individual importances of 4 per cent each, while several Pacific–Kula profiles have the lowest individual importance of 0.1 per cent each.

We can further approximately separate the information contribution of the data into their pole and anomalous skewness components. To examine how the data contribute to the pole position, we re-inverted the data while constraining anomalous skewness to equal its best-fitting value of 16.2°. In this inversion the importances sum to two and only reflect the information contribution to the pole position conditional on anomalous skewness being perfectly

known, and thus ignoring the covariance between the pole position and anomalous skewness. In this numerical experiment, the central Pacific–Farallon data contribute 44 per cent of the information constraining the pole, the northern Pacific–Farallon data 29 per cent, the southern Pacific–Farallon data 18 per cent, the Pacific–Kula data 5 per cent, and the Pacific–Bellingshausen and Pacific–Antarctic data 3 per cent. In the complementary numerical experiment, fixing the pole position at its best-fitting location, the importances sum to one and only reflect the information contribution to anomalous skewness, again ignoring the covariance between pole position and anomalous skewness. In this case, the northern Pacific–Farallon data contribute 33 per cent of the information constraining anomalous skewness, the Pacific–Kula data 23 per cent, the Pacific–Antarctic data 14 per cent, the southern Pacific–Farallon data 12 per cent, the Pacific–Bellingshausen data 9 per cent, and the central Pacific–Farallon data 8 per cent. We conclude that the Pacific–Farallon data mainly constrain the pole position, while the northern Pacific–Farallon and Pacific–Kula data contain over half of the anomalous skewness information.

### Dependence of anomalous skewness on spreading rate

Anomalous skewness depends on spreading rate (Cande 1976, 1978; Arkani-Hamed 1988; Roest *et al.* 1992). Our anomalous skewness estimate is consistent with the trend of anomalous skewness versus spreading rate found by Roest *et al.* (1992), which is unsurprising as their results included

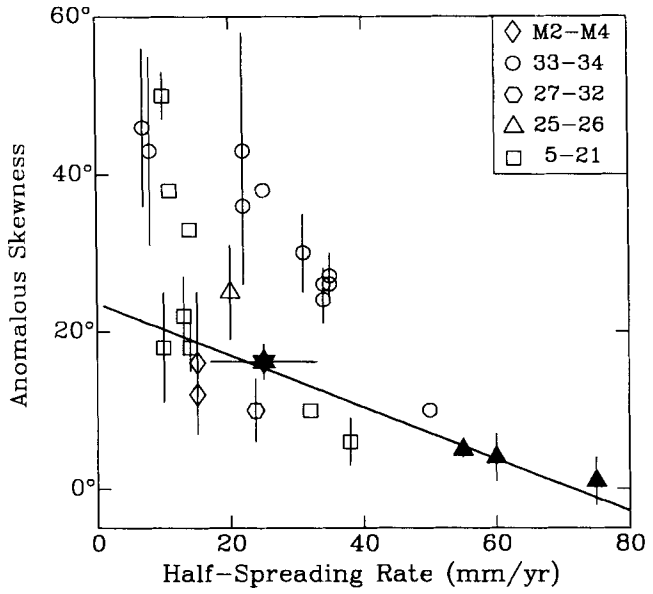


**Figure 18.** Dependence of anomalous skewness on spreading rate as inferred from the results of many studies. Slow spreading rates tend to have higher values of anomalous skewness for a given anomaly than do fast spreading rates. The vertical bars show one standard deviation. The values most relevant to the present paper, i.e. those from the sequence of anomalies 25, 25r and 26, are shown by solid triangles. Our estimate is shown by a solid star. The horizontal bars on the 25r datum span the range of spreading rates estimated from our profiles. The solid line represents a least-squares straight line fit to the 25r and 25–26 data (see eq. 11). After Roest *et al.* (1992).

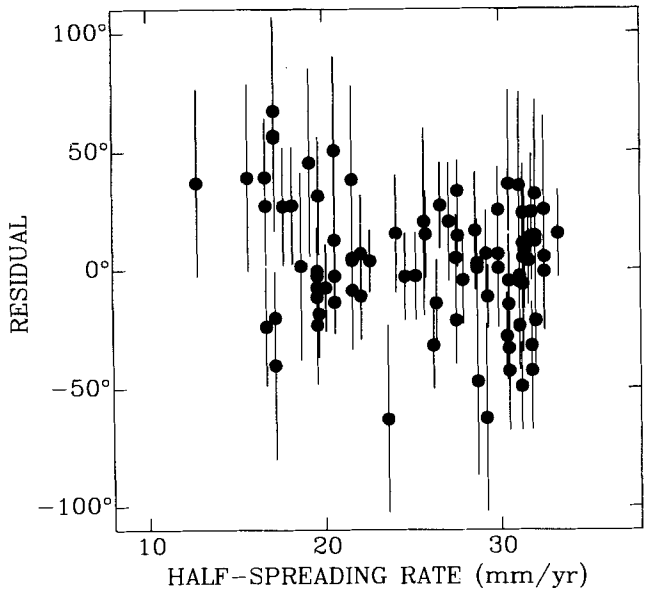


**Figure 19.** Effective remanent inclination residuals versus half-spreading rate for each profile used in the pole calculation. The best-fitting straight line through these data has a statistically insignificant slope of $-0.41° \pm 0.78°$ (mm yr$^{-1}$)$^{-1}$.

preliminary results from our work (Fig. 18). To examine how large an effect this dependence has on our skewness estimates, we analysed the residuals of apparent effective remanent inclination as a function of spreading rate (Fig. 19). The straight line that best fits these data has a statistically insignificant slope of $-0.41° \pm 0.78°$ (95 per cent confidence limits) per each mm yr$^{-1}$ change in half-spreading rate with a reduced chi-square of 1.06. Thus, it would appear that over the range in half-spreading rates observed for the Pacific plate during chron 25r, the variation in anomalous skewness has a small effect on the pole.

To quantify the effect on our pole of spreading-rate dependence we performed an additional pole calculation assuming different values of anomalous skewness for different spreading rates. The form of the dependence of anomalous skewness on spreading rate is not yet well understood. Thus, we treated this dependence phenomenologically. We fit a straight line by least squares to estimates of anomalous skewness versus half-spreading rate for anomalies 25–26 estimated by Roest *et al.* (1992) plus our new result. We omitted one estimate of theirs lacking an across-ridge comparison. We weighted the estimates of anomalous skewness inversely to their standard errors (Fig. 18). The empirical best-fit is described by the following equation:

$$\theta_a = 23.58° - 0.330u, \quad (11)$$

where $u$ is the half-spreading rate in mm yr$^{-1}$. This calculated trend suggests a 5° variation in anomalous skewness over the range of observed Pacific half-rates (17–33 mm yr$^{-1}$). We then adjusted each of our apparent effective remanent inclinations for the appropriate anomalous skewness, which depended on the spreading rate determined for that profile. For profiles where no estimated spreading rate was available, we interpolated between rates

of neighbouring profiles. For this adjusted data set, the pole is located at 77.6°N, 3.6°E with a 95 per cent confidence ellipse that has a 6.5° major semi-axis striking N91°E and a 4.0° minor semi-axis. This pole differs by a statistically insignificant 0.6° from the one calculated assuming constant anomalous skewness and gives a value of $\chi^2$ of 131.3, insignificantly greater than the value of 128.6 obtained when no correction for spreading rate is applied. The intercept of this curve (i.e. the constant term 23.58°) has no effect on the resulting calculation as we solved for $\theta_a$ when determining the pole. The nominal value of anomalous skewness is $0.7° \pm 4.6°$ (95 per cent confidence level). Because the anomalous skewness trend used to adjust the effective inclinations is not yet very well constrained, and because the empirical adjustments lead to an increase in chi-square, our preferred pole remains the one that was calculated assuming anomalous skewness is independent of spreading rate.

### Pacific apparent polar wander

The age (~57 Ma) of the new chron 25r pole lies within the 26 myr long age gap between published 39 Ma (Sager 1987) and 65 Ma (Acton & Gordon 1991) poles for the Pacific plate. Its location suggests that the Pacific plate moved $11.5° \pm 3.4°$ (95 per cent confidence limits) northward since 57 Ma. When compared with the locations of neighbouring poles on the APW path, it suggests rapid northward APW ($0.83°$ Myr $\pm 0.46°$ Myr) from 65 to 57 Ma, continuing the trend of rapid APW from 80 to 65 Ma (Gordon 1982), and statistically insignificant southward APW ($0.05°$ Myr $\pm$ $0.28°$ Myr) from 57 to 39 Ma (Fig. 20). The large amount of northward motion since 82 Ma (>30°) combined with the modest northward motion since 57 Ma (11°) strongly suggests that about two-thirds of the post-Mid Cretaceous northward motion of the Pacific plate occurred during the 25 Myr interval from 82 to 57 Ma.

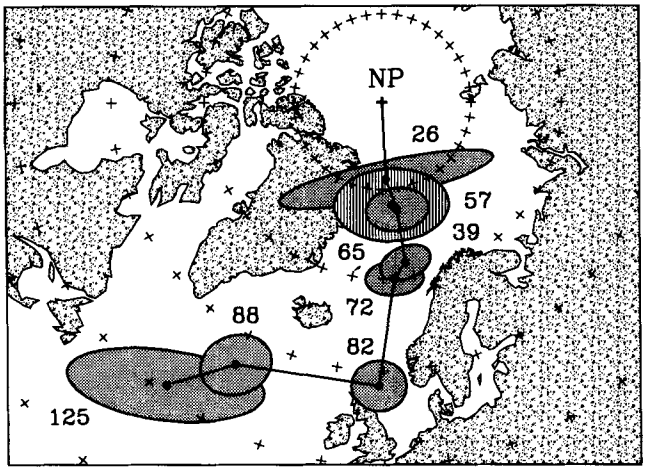


**Figure 20.** Apparent polar wander path of the Pacific plate. The poles shown are a 125 Ma pole (Petronotis *et al.* 1992), 72 Ma, 82 Ma and 88 Ma poles (Sager & Pringle 1988), a 65 Ma pole (Acton & Gordon 1991), the 57 Ma pole calculated here, a 39 Ma pole (Sager 1987), and a 26 Ma pole (Acton & Gordon 1994) calculated from palaeolatitude data. The latitude of the chron 25r pole shows that the Pacific plate has moved $11.5° \pm 3.4°$ northward since 57 Ma. When compared with the locations of neighbouring poles on the APW path, it suggests rapid northward APW ($0.83°$ Myr $\pm 0.46°$ Myr) from 65 to 57 Ma and statistically insignificant southward APW ($0.05°$ Myr $\pm 0.28°$ Myr) from 57 to 39 Ma. (Stereographic projection, tick marks every 10°.)

### Timing and rate of the latitudinal shift of the Hawaiian hotspot

The Hawaiian hotspot has shifted ~8° southward during Cainozoic time (Kono 1980; Gordon & Cape 1981), but the rate and timing of the shift are poorly known. Little, if any, net shift has occurred during the past 39 million years (Gordon & Cape 1981; Sager 1983, 1987; Suárez & Molnar 1980).

In Fig. 21 we show the northward motion of the Pacific plate indicated by different types of data including dated seamounts and islands along the Hawaiian–Emperor chain, palaeomagnetic data such as inclinations from azimuthally unoriented sediment piston cores, and sediment facies data that record the passage of the plate through the biogenically rich equatorial zone. In addition to data compiled by Gordon & Cape (1981), we have added several palaeolatitudes (Epp *et al.* 1983), a 39 Ma pole (Sager 1987), the 57 Ma skewness pole determined here, a 65 Ma pole (Acton & Gordon 1991), and 72 Ma, 82 Ma and 88 Ma poles (Sager & Pringle 1988) determined from seamount, palaeocolatitude, amplitude and skewness data. A comparison of the northward motion indicated by the different types of data suggests that before 39 Ma the hotspot data

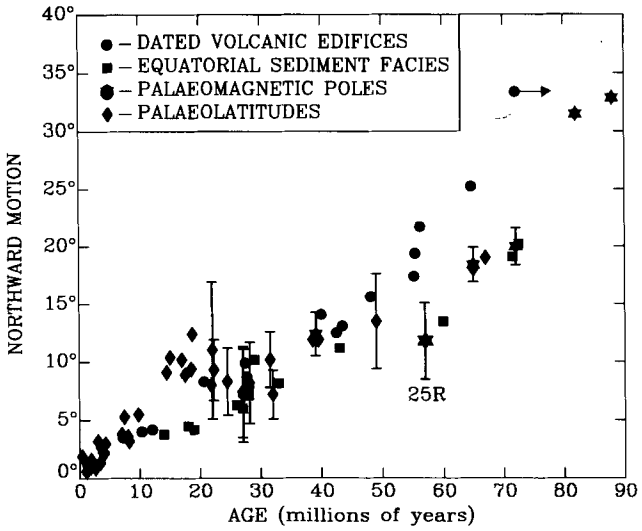


**Figure 21.** Northward motion of the Pacific plate inferred from dated seamounts and islands of the Hawaiian–Emperor chain (●), palaeomagnetic poles (▲), palaeolatitudes (◆), and equatorial sediment facies data (■). The error bars on the 39, 57, 65 and 72 Ma poles are 1-D 95 per cent confidence limits of northward motion estimated using the following reference seamounts in the Hawaiian–Emperor chain: Abbott seamount ($38.7 \pm 0.9$ Ma, Clague & Dalrymple 1989) for 39 Ma, Nintoku seamount ($56.2 \pm 0.6$ Ma, Clague & Dalrymple 1989) for 57 Ma, and Suiko seamount ($64.7 \pm 1.1$ Ma, Clague & Dalrymple 1989) for 65 and 72 Ma. The arrow on the 72 Ma hotspot datum (Meiji guyot) indicates that this date is considered to be a minimum age. After Gordon & Cape (1981).

disagree with the palaeomagnetic and equatorial sediment facies data. The consistency of the palaeomagnetic with the equatorial sediment facies data over the earlier time interval excludes the presence of large non-dipole components of the palaeomagnetic field. The northward motion suggested by the 57 Ma pole is also consistent with the sparse sediment facies data. All the data may be best explained by no southward drift of the Hawaiian hotspot from ~70 to 57 Ma followed by a southward drift of the hotspot confined to the interval 57–39 Ma. The shift may coincide with a global shift of all hotspots relative to the spin axis (Morgan 1981; Gordon & Cape 1981), but has other possible explanations, including motion between hotspots. Using the values shown on Fig. 21, and neglecting the uncertainties in the ages of the dated seamounts, we find that the Hawaiian hotspot has drifted southward by $10.2° \pm 3.4°$ since 57 Ma, but only by $1.7° \pm 1.9°$ since 39 Ma. This gives a southward displacement of $8.5 \pm 3.9°$ (95 per cent confidence limits) between 57 and 39 Ma, corresponding to a rate of southward motion of $52 \pm 24$ mm yr$^{-1}$. Incorporation of realistic age uncertainties, however, would increase these uncertainties considerably. We hope in future work to obtain more poles in the gap from 57 to 39 Ma to improve estimates of the timing and rate of the southward drift of the hotspot.

### Prospects for improving the Pacific APW path with further study of skewness

Our results strongly suggest that we have obtained a reliable, precisely dated palaeomagnetic pole with usefully compact confidence limits from a data set with 149 total (132 useful) sampling locations spanning a distance exceeding 11 000 km. Introducing anomalous skewness as an adjustable parameter gives a highly significant reduction in the variance of the data, and brings the skewness great semicircles of most regions of the Pacific plate into consistency.

We believe, therefore, that the prospects for obtaining additional accurate precisely dated poles with this approach are excellent not only for older Cainozoic and Late Cretaceous anomalies, which can incorporate skewnesses from profiles over Pacific–Kula spreading, but also younger anomalies, since the information contribution from the Pacific–Kula profiles sums only to 8 per cent. We expect that the dispersion of skewness estimates is likely to be smaller for anomalies over sea-floor formed during long chrons than during short chrons, because the shape of anomalies corresponding to long chrons seems less likely to be affected by various noise sources. If true, particularly promising anomalies to study include 12r, 18, 20–21, 24r, 26r, 30/31, 32, 33n and 33r, with many other anomalies being suitable for study as well. If future results are as encouraging as the present results, an accurate, high-resolution apparent polar wander path can be determined for the Pacific and other oceanic plates by analysis of the shapes of additional marine anomalies using the same method of analysis.

The profiles north of the Galapagos fracture zone and south of the Molokai fracture zone contribute 32 per cent of the information contained in the pole and anomalous skewness. This strongly suggests that the accuracy of the chron 25r pole, as well as poles of other ages, could be greatly improved by collection and analysis of magnetic field intensity measurements on profiles parallel to palaeo-plate-motion flow lines in this sparsely surveyed but accessible region.

## CONCLUSIONS

By analysing the shape of 132 useful (149 total) crossings of anomaly 25r we have obtained a precisely date chron 25r (56.5–57.8 Ma) Pacific-plate palaeomagnetic pole with usefully compact confidence limits. The variation of anomalous skewness over the range of spreading rates encountered in the Pacific plate during this time interval has a negligible effect on the pole. Therefore, it seems worthwhile to attempt further skewness analyses to estimate usefully accurate, precisely dated palaeomagnetic poles, each of which is determined from many crossings of a single anomaly. Comparison of the new pole with other palaeomagnetic data and with equatorial sediment-facies data, indicates that two-thirds (i.e. ~20°) of the post-mid Cretaceous northward motion of the Pacific plate occurred between 80 and 57 Ma, with negligible northward motion from 57 to 39 Ma, and slow northward motion since 39 Ma. Comparison of these data with the northward motion inferred from dated volcanoes along the Hawaiian–Emperor seamount chain indicates little southward motion of the Hawaiian hotspot between ~70 and 57 Ma, $8.5° \pm 3.9°$ (95 per cent confidence limits) of southward motion from 57 to 39 Ma, and insignificant southward motion since 39 Ma.

## ACKNOWLEDGMENTS

We thank Steve Cande for his thoughtful review. This work was supported by National Science Foundation grants EAR-9205875 (K.E.P.), EAR-9005679 (R.G.G.) and OCE-9019318 (G.D.A.), and by the Caswell Silver Foundation while G.D.A. was at the University of New Mexico.

## REFERENCES

Acton, G.D. & Gordon, R.G., 1991. A 65 Ma palaeomagnetic pole for the Pacific Plate from the skewness of magnetic anomalies 27r–31, *Geophys. J. Int.*, **106,** 407–420.

Acton, G.D. & Gordon, R.G., 1994. Paleomagnetic tests of Pacific plate reconstructions and implications for motion between hotspots, *Science*, **263,** 1246–1254.

Arkani-Hamed, J., 1988. Remanent magnetization of the oceanic upper mantle, *Geophys. Res. Lett.*, **15,** 48–51.

Arkani-Hamed, J., 1990. Magnetization of the oceanic crust beneath the Laborador Sea, *J. geophys. Res.*, **95,** 7101–7110.

Atwater, T. & Severinghaus, J., 1989. Tectonic maps of the northeast Pacific, in *The Eastern Pacific Ocean and Hawaii, The Geology of North America*, Vol. N, eds Winterer, E.L., Hussong, D.M. & Decker, R.W., Geological Society of America, Boulder, CO.

Blakely, R.J., 1976. An age dependent, two layer model for marine magnetic anomalies, in *The Geophysics of the Pacific Ocean Basin and Its Margin*, pp. 227–234, Geophys. Monogr. Ser. 19, eds Sutton, G.H., Manghnani, M.H. & Moberly, R., Am. geophys. Un., Washington, DC.

Blakely, R.J. & Lynn, W.S., 1977. Reversal transition widths and fast-spreading centers, *Earth planet. Sci. Lett.*, **33,** 321–330.

Cande, S.C., 1976. A palaeomagnetic pole from Late Cretaceous

marine magnetic anomalies in the Pacific, *Geophys. J. R. astr. Soc.*, **44,** 547–566.

Cande, S.C., 1978. Anomalous behavior of the paleomagnetic field inferred from the skewness of anomalies 33 and 34, *Earth planet. Sci. Lett.*, **40,** 275–286.

Cande, S.C. & Haxby, W.F., 1991. Eocene propagating rifts in the southwest Pacific and their conjugate features on the Nazca plate, *J. geophys. Res.*, **96,** 19 609–19 622.

Cande, S.C. & Kent, D.V., 1976. Constraints imposed by the shape of marine magnetic anomalies on the magnetic source, *J. geophys. Res.*, **81,** 4157–4162.

Cande, S.C. & Kent, D.V., 1992. A new geomagnetic polarity time scale for the Late Cretaceous and Cenozoic, *J. geophys. Res.*, **97,** 13 917–13 951.

Cande, S.C. & Kristoffersen, Y., 1977. Late Cretaceous magnetic anomalies in the North Atlantic, *Earth planet. Sci. Lett.*, **35,** 215–224.

Christoffel, D.A. & Falconer, R.K.H., 1972. Marine magnetic anomalies in the South-west Pacific Ocean and the identification of new tectonic features, in *Antarctic Oceanology II; The Australian–New Zealand Sector*, pp. 197–209, Antarctic Res. Ser., 19, ed. Hayes, D.E., Am. geophys. Un., Washington, DC.

Clague, D.A. & Dalrymple, G.B., 1989. Tectonics, geochronology, and origin of the Hawaiian–Emperor volcanic chain, in *The Geology of North America: The Eastern Pacific Ocean and Hawaii*, Vol. N, pp. 188–217, eds Winterer, E.L., Hussong, D.M. & Decker, R.W., GSA, Boulder, CO.

Engebretson, D.C., Cox, A. & Gordon, R.G., 1984. Relative motions between oceanic plates of the Pacific basin, *J. geophys. Res.*, **89,** 10 291–10 310.

Epp, D., Sager, W.W., Theyer, F. & Hammond, S.R., 1983. Hotspot-spin axis motion or magnetic far-sided effect, *Nature*, **303,** 318–320.

Gordon, R.G., 1982. The late Maastrichtian palaeomagnetic pole of the Pacific plate, *Geophys. J. R. astr. Soc.*, **70,** 129–140.

Gordon, R.G. & Cape, C.D., 1981. Cenozoic latitudinal shift of the Hawaiian hotspot and its implications for true polar wander, *Earth planet. Sci. Lett.*, **55,** 37–47.

Grim, P.J. & Erickson, B.H., 1969. Fracture zones and magnetic anomalies south of the Aleutian Trench, *J. geophys. Res.*, **74,** 1488–1494.

Hayes, D.E. & Heirtzler, J.R., 1968. Magnetic anomalies and their relation to the Aleutian Island Arc, *J. geophys. Res.*, **73,** 4637–4646.

Kono, M., 1980. Paleomagnetism of DSDP leg 55 basalts and implications for the tectonics of the Pacific plate, *Initial Rep. Deep Sea Drill. Proj.*, **55,** 737–752.

Kruse, S.E., 1988. Magnetic lineations on the flanks of the Marquesas swell: Implications for the age of the seafloor, *Geophys. Res. Lett.*, **15,** 573–576.

Lonsdale, P., 1988. Paleogene history of the Kula plate: Offshore evidence and onshore implications, *Geol. Soc. Am. Bull.*, **100,** 733–754.

Macdonald, K.C., Haymon, R.M., Miller, S.P., Sempere, J.-C. & Fox, P.J., 1988. Deep-tow and sea beam studies of dueling propagating ridges of the East Pacific Rise near 20°40′S, *J. geophys. Res.*, **93,** 2875–2898.

Mayes, C.L., Lawver, L.A. & Sandwell, D.T., 1990. Tectonic history and new isochron chart of the South Pacific, *J. geophys. Res.*, **95,** 8543–8567.

Morgan, W.J., 1981. Hot spot tracks and the opening of the Atlantic and Indian Oceans, in *Oceanic Lithosphere*, Vol. 7, *The Sea*, pp. 443–487, ed. Emiliani, C., Wiley-Interscience, New York.

Petronotis, K.E. & Gordon, R.G., 1989. Age dependence of skewness of magnetic anomalies above seafloor formed at the Pacific–Kula spreading center, *Geophys. Res. Lett.*, **16,** 315–318.

Petronotis, K.E., Gordon, R.G. & Acton, G.D., 1992. Determining palaeomagnetic poles and anomalous skewness from marine magnetic anomaly skewness data from a single plate, *Geophys. J. Int.*, **109,** 209–224.

Prince, R.A., Heath, G.R. & Kominz, M., 1980. Palaeomagnetic studies of central North Pacific sediment cores: stratigraphy sedimentation rates, and the origin of the magnetic instability, *Geol. Soc. Am. Bull.*, **91,** 1789–1835.

Raymond, C.A. & LaBrecque, J.L., 1987. Magnetization of the oceanic crust: Thermoremanent magnetization or chemical remanent magnetization?, *J. geophys. Res.*, **92,** 8077–8088.

Roest, W.R., Arkani-Hamed, J. & Verhoef, J., 1992. The seafloor spreading rate dependence of the anomalous skewness of marine magnetic anomalies, *Geophys. J. Int.*, **109,** 653–669.

Rosa, J.C.C. & Molnar, P., 1988. Uncertainties in reconstructions of the Pacific, Farallon, Vancouver, and Kula plates and constraints on the rigidity of the Pacific and Farallon (and Vancouver) plates between 72 and 35 Ma, *J. geophys. Res.*, **93,** 2997–3008.

Sager, W.W., 1983. A late Eocene paleomagnetic pole for the Pacific plate, *Earth planet. Sci. Lett.*, **63,** 408–422.

Sager, W.W., 1987. Late Eocene and Maastrichtian paleomagnetic poles for the Pacific plate: implications for the validity of seamount paleomagnetic data, *Tectonophysics*, **144,** 301–314.

Sager, W.W. & Pringle, M.S., 1988. Mid-Cretaceous to early Tertiary apparent polar wander path of the Pacific plate, *J. geophys. Res.*, **93,** 11 753–11 771.

Schouten, H., 1971. A fundamental analysis of magnetic anomalies over oceanic ridges, *Mar. geophys. Res.*, **1,** 111–114.

Schouten, H. & Cande, S.C., 1976. Palaeomagnetic poles from marine magnetic anomalies, *Geophys. J. R. astr. Soc.*, **44,** 567–575.

Schouten, H. & McCamy, K., 1972. Filtering marine magnetic anomalies, *J. geophys. Res.*, **77,** 7089–7099.

Stock, J. & Molnar, P., 1982. Uncertainties in the relative positions of the Australia, Antarctica, Lord Howe, and Pacific plates since the Late Cretaceous, *J. geophys. Res.*, **87,** 4697–4714.

Stock, J. & Molnar, P., 1987. Revised history of early Tertiary plate motion in the south-east Pacific, *Nature*, **325,** 495–499.

Suárez, G. & Molnar, P., 1980. Paleomagnetic data and pelagic sediment facies and motion of the Pacific plate relative to the spin axis since the Late Cretaceous, *J. geophys. Res.*, **85,** 5257–5280.

Verosub, K.L. & Moores, E.M., 1981. Tectonic rotations in extensional regimes and their paleomagnetic consequences for oceanic basalts, *J. geophys. Res.*, **86,** 6335–6349.

Weissel, J.K. & Hayes, D.E., 1972. Magnetic anomalies in the southeast Indian Ocean, in *Antarctic Oceanology II: The Australian–New Zealand Sector*, pp. 165–196, Antarctic Res. Ser., 19, ed. Hayes, D.E., Am. geophys. Un., Washington, DC.